Augmented prediction of multi-species protein–RNA interactions using evolutionary conservation of RNA-binding proteins

Jiale He[1,*], Tong Zhou[1,*], Lu-Feng Hu[2,3,*], Yuhua Jiao[1], Junhao Wang[1], Shengwen Yan[1], Siyao Jia[1], Qiuzhen Chen[1], Wentao Zhu[1], Jilin Zhang[4], Mutian Jia[5], Yuanning Li[6], Xianwei Wang[1,9], Yangming Wang[2,3], Yucheng T. Yang[7,8,#], Lei Sun[1,9,#]

[1] Shandong Provincial Key Laboratory of Animal Cell and Developmental Biology, School of Life Sciences, Shandong University, Qingdao 266237, China

[2] State Key Laboratory of Gene Function and Modulation Research, Institute of Molecular Medicine, College of Future Technology, Peking University, Beijing 100871, China

[3] Beijing Advanced Center of RNA Biology (BEACON), Peking University, Beijing 100871, China

[4] Department of Biomedical Sciences, College of Biomedicine, City University of Hong Kong, Kowloon Tong, Hong Kong SAR 999077, China

[5] Key Laboratory of Infection Immunity and Disease Intervention of Shandong Province, Key Laboratory for Experimental Teratology of Ministry of Education, Department of Immunology, School of Basic Medical Science, Cheeloo College of Medicine, Shandong University, Jinan, Shandong, 250012, China

[6] Institute of Marine Science and Technology, Shandong University, Qingdao, 266237, China

[7] College of Biomedical Engineering, Fudan University, Shanghai 200438, China

[8] MOE Key Laboratory of Computational Neuroscience and Brain-Inspired Intelligence, and MOE Frontiers Center for Brain Science, Fudan University, Shanghai 200433, China

[9] State Key Laboratory of Microbial Technology, Shandong University, Qingdao 266237, China

*These authors contributed equally to this work

#Correspondence: yangyy@fudan.edu.cn (Y.T.Y.); sunlei0227@sdu.edu.cn (L.S.)

Highlights

- MuSIC integrates RBP-binding peaks with conservation-weighted label smoothing to predict RBP–RNA interactions across eleven species
- MuSIC outperforms state-of-the-art computational methods in predicting cross-species RBP–RNA interactions
- Cross-species prediction accuracy of RBP-binding peaks correlates with the conservation of RBPs
- MuSIC quantifies the effects of homologous SNVs on RBP binding with experimental validation in mouse

Abstract

RNA-binding proteins (RBPs) play critical roles in gene expression regulation. Recent studies have begun to detail the RNA recognition mechanisms of diverse RBPs. However, given the array of RBPs studied so far, it is implausible to experimentally profile RBP-binding peaks for hundreds of RBPs in multiple non-model organisms. Here, we introduce MuSIC (**Mu**lti-**S**pecies RBP–RNA **I**nteractions using **C**onservation), a deep learning-based framework for predicting cross-species RBP–RNA interactions by leveraging label smoothing and evolutionary conservation of RBPs across 11 diverse species ranging from human to yeast. MuSIC outperforms state-of-the-art computational methods, and provides predicted RBP-binding peaks across species with high accuracy. The prediction confidence is higher in the closely related species, partially due to the RBP conservation patterns. Finally, the effects of homologous genetic variants on RBP binding can be computationally quantified across species, followed by experimental validations. The target transcripts with disrupted binding events are enriched with the ubiquitination-associated pathways. To summarize, MuSIC provides a useful computational framework for predicting RBP–RNA interactions cross-species and quantifying the effects of genetic variants on RBP binding, offering novel insights into the RBP-mediated regulatory mechanisms implicated in human diseases.

Keywords

RBP–RNA interaction, deep learning, protein conservation, cross-species prediction, post-transcriptional regulation

Introduction

RNA-binding proteins (RBPs) play an important role that interact with intracellular RNAs by recognizing specific RNA motifs, and perform important biological functions including RNA transcription, splicing, transport, translation, and stability [1–3]. Disruptions in RBP–RNA interactions have been implicated in the pathogenesis of various diseases, particularly cancer and neurodegenerative diseases [4,5].

Genetic variants, including single nucleotide polymorphisms (SNPs) and single nucleotide variants (SNVs), can alter the RBP-binding affinity, thereby disrupting RNA recognition and contributing to the development of various diseases [6–8]. For example, the genetic variants in the iron-responsive element of *FTL* can impair the binding of IRP1 to *FTL* mRNA, leading to hyperferritinaemia-cataract syndrome [9]. Similarly, the genetic variants in *TCF3* can hinder the binding of hnRNPH1 to exon 18b, thus disrupting alternative splicing of *TCF3* and promoting Burkitt lymphoma development [10]. These cases highlight the critical roles of RBP–RNA interactions in human disease pathogenesis.

Model organisms, such as mouse and zebrafish, are widely used in revealing the pathogenic mechanisms of complex human diseases[11,12], where normal RBP–RNA interactions could be potentially disrupted by genetic variants [13,14]. Various high-throughput experimental methods have been applied to identify RBP-binding peaks both *in vitro* [15–17] and *in vivo* [18–21] . For example, PAR-CLIP technology has been applied to the mouse for exploring the regulatory roles of IGF2BP3 and LIN28B in hematopoietic reprogramming [22]. However, it is still unrealistic to generate the binding profiles of hundreds of RBPs in human and animal models using *in vivo* high-throughput experimental methods.

With the recent advancements in AI technologies, computational methods leveraging large-scale RBP–RNA binding data can effectively learn RBP binding characteristics [19,23,24]. Several computational methods using machine learning [25,26] and deep learning [27–31] technologies have been developed to predict RBP-binding peaks and model their RNA sequence preferences. However, the predictions by these traditional computational methods are generally restricted in the specific species, where the CLIP-seq datasets are generated. Given the fact that only a minority of the RBPs that have been studied by CLIP-seq technologies are from non-human organisms—65 RBPs identified in yeast, 45 in mouse, and only 5-6 in species such as fly, worm, and *A. thaliana* [32], it is vital to develop novel computational methods to predict RBP–RNA interactions in the cross-species tasks[33,34].

The style transfer methods have been successfully applied in the field of computer vision, where similarity-guided label smoothing strategy could improve the cross-style performance [35–37]. In our study, the analogies of the similarity features in label smoothing can be the sequence and structural conservation of RBPs. RBPs have been shown to be relatively highly conserved across species, particularly for the core RNA-binding domains (RBDs) [38–40]. Consistently, the RBP-binding motifs from the RBPs containing highly conserved RBDs also show notable degree of conservation [41–43]. These observations inspire us to apply the label smoothing strategy to the prediction of cross-species RBP–RNA interactions.

In this study, we develop MuSIC (**Mu**lti-**S**pecies RBP–RNA **I**nteractions using **C**onservation), a deep learning framework for cross-species RBP–RNA interaction prediction by leveraging the multi-level conservation patterns of RBPs. We show that MuSIC can accurately predict RBP-binding peaks across species and outperforms existing state-of-the-art computational methods, particularly in the closely related species. We then apply MuSIC to systematically profile the RBP-binding peaks and motifs for 186 RBPs across 11 species. Finally, we use MuSIC to quantify the effects of SNVs on RBP binding, providing insights into the RBP-mediated regulatory mechanisms associated with human diseases.

Results

Evolutionarily conserved RBPs exhibit similar RNA-binding preference

Previous studies have revealed that RBDs, the core functional elements in RBPs, exhibit a significantly slower rate of sequence evolution compared to genomic sequence context surrounding these RBDs, indicating their critical functions in regulating RNA recognition [38]. We collected protein sequences and predicted structures of 216 RBPs from 11 species ranging from human to yeast, including human, orangutan, monkey, mouse, rat, chicken, frog, zebrafish, fly, *A. thaliana* and yeast, to systematically assess the conservation patterns of RBPs and their core RBDs (see **Methods** for details). Briefly, the conservation patterns of RBPs and their core RBDs was evaluated based on sequence and structure similarity, respectively (**Fig. 1a**, **Supplementary Fig. 1** and **Supplementary Table 1**). As expected, both sequence and structural similarities between human and non-human species declined with the increasing evolutionary distance (**Fig. 1a**). In particular, the protein sequence exhibited higher conservation for the core RBDs compared to the full-length RBPs; however, the structural similarity for both core RBDs and full-length RBPs remained relatively high across the 11 species ranging from human to yeast (**Fig. 1a** and **Supplementary Fig. 1**), indicating the fundamental importance of local structures of core RBDs for RNA recognition.

We then sought to partition the 216 RBPs into different groups based on their conservation patterns across the 11 species (**Supplementary Table 2**) and showed cases in each group (**Fig. 1b**): (i) highly conserved (1169, accounting for 49.0%), showing conservation in both sequence and structure in closely related species such as human and mouse, exemplified with the case of AGO2 protein; (ii) considerable conserved (769, accounting for 32.2%), showing conservation in full-length and RBD structure, such as DDX51; (iii) intermediately conserved (426, accounting for 17.8%), showing conservation in only RBD structure, such as RBM10; and (iv) weakly conserved (23, accounting for 1.0%), such as SERBP1. We found that almost all the RBPs (>99% of the total) exhibit structural conservation in their RBDs, consistent with previous studies showing that RBDs of the same RBP are highly structurally conserved across species [44,45].

Previous studies have shown that RBPs containing structurally conserved RBDs tend to recognize and bind their RNA target with similar sequence patterns [41,45,46]. We first compared the distribution of RBP-binding peaks from the homologous RBPs along mRNAs in human and mouse, exemplified with the case of SRRM4 and LIN28A (**Fig. 1c** and **Supplementary Fig. 2a**). As expected, we observed a high correlation of the RBP-binding peak distributions between human and mouse (SRRM4 $r = 0.96$, LIN28A $r = 0.91$, Spearman's rank correlation test). Notably, SRRM4 showed stronger preference of binding on the stop codon and a depletion around the start codon (**Fig. 1c**), suggesting the critical roles of SRRM4 in regulating alternative splicing of RNA within these regions [47]. Next, we explored the motif-level conservation of RBPs using the ATtRACT database [48], which contains experimentally validated binding motifs in multiple species. Comparative analysis of RBP-binding motifs between human and mouse revealed a high degree of conservation (e.g., UUCUGUG motif for RC3H1, GGGGGCUG motif for HNRNPF, GGAG motif for LIN28A) (**Fig. 1d**). Moreover, both the structures derived from X-ray diffraction (**Fig. 1e**) and AlphaFold3 [49] prediction (**Supplementary Fig. 2b-e**) suggest that the homologous RBPs from different species exhibit similar three-dimensional interaction patterns between the interface residues in RBPs and their recognized target binding motifs (PDB ID 4QIL in human and 4QI2 in mouse) (**Fig. 1e**). Taken together, these results suggest that RBPs show high sequence and structural conservation across species, and maintain high conservation in their RNA-binding patterns, including motifs, binding regions within transcripts, and key interacting residues.

Inspired by the aforementioned observations and previous studies[30,33,43], we aim to develop a novel computational model to systematically predict the RBP–RNA interactions in the target species (e.g., non-human species) by integrating the RBP-binding peaks from the source species (e.g., human) and the RBP similarity patterns between species. We leveraged the large-scale RBP-binding peaks from different species (human, mouse, and zebrafish) to construct the computational model. We initially found 23 homologous RBPs between human and mouse, and one homologous RBP between human and zebrafish with available datasets from POSTAR3

(**Supplementary Fig. 2f**), among which 38 datasets from 14 RBPs were curated for the training and validation of the cross-species model (see **Methods** for details; **Supplementary Table 3**).

Overview of MuSIC algorithm

We developed MuSIC, a deep learning framework that could integrate RBP-binding peaks and cross-species conservation information of RBPs to accurately model and predict RBP–RNA interactions in diverse non-human species. Briefly, the MuSIC framework consists of four components (**Fig. 2a**): (i) pre-processing input data: collecting peaks of RBPs from multiple species, and constructing training and validation sets; (ii) feature engineering: incorporating nucleotide sequences and RNA secondary structures to learn RBP-binding preferences and enhance the prediction ability of the model (**Fig. 2b**); (iii) predicting RBP–RNA interactions**:** dynamic optimization on the prediction results using label smoothing regularization and gradient weight adaptation in a convolutional neural network (CNN); and (iv) analyzing RBP–RNA interactions: cross-species motif identification and other downstream applications.

We realized that the cross-species prediction tasks often have great challenges in generalization, e.g., the ability to accurately predict RBP–RNA interactions in mouse based on the same distribution as the training data in human [33,34]. There are several disadvantages in the existing deep learning-based methods, such as overfitting caused by the limitations of one-hot label loss functions, and heightened sensitivity to label noise and boundary ambiguities inherent in one-hot supervision [36]. To this end, we leveraged the label smoothing strategy that has been widely used in the field of computer vision to facilitate the cross-style classification [35]. In MuSIC, the conservation of RBPs across species can be used to enhance the model generalization and mitigate overfitting in a similar way. Briefly, MuSIC employs a novel approach in applying the label smoothing strategy, in which the one-hot labels were converted into soft labels based on the pre-defined RBP conservation scores [37]. The cross-entropy loss was computed for both label types, with the final loss obtained by weighting and summing the two components (**Fig. 2c**). In addition, we used gradient weight adaptation algorithm to dynamically adjust the weight of each loss component during the model training (**Fig. 2d**). Next, the MuSIC model combines several convolutional layers, residual blocks and the Squeeze-and-Excitation (SE) module to capture and enhance RBP binding features learning, in which overfitting could be minimized by dropout and early stopping (**Fig. 2a, e**). Finally, the learned features were integrated using the fully connected layers to generate the prediction outputs (see **Methods** for details).

Existing state-of-the-art computational methods typically utilize input sequence lengths of 101nt [28,30,31] or 400nt [26,50]. We found that increasing the input sequence length to 200nt could significantly improve the Area Under the Curve (AUC) score in cross-species prediction (**Fig. 2f** and **Supplementary Fig. 3a**). The inclusion of label smoothing, and gradient adaptation could further improve the AUC score (**Fig. 2f** and **Supplementary Fig. 3b**). Notably, incorporating predicted RNA structures could further enhance the AUC score to 0.85 in cross-species prediction (**Fig. 2f**). We also evaluated the prediction performance using the experimentally measured *in vivo* RNA structures instead of the predicted RNA structures (**Supplementary Fig. 3c**). The predicted RNA structures were used in the model because of the limited performance gains by using the *in vivo* RNA structures, as well as very few *in vivo* RNA structure datasets are available in other species. Taken together, these results reveal that extending the sequence length and applying label smoothing could significantly improve the performance of cross-species generalization.

We then characterized the contribution of each component of the MuSIC framework to the performance of feature learning. The positive and negative samples of input RNA sequences cannot be clearly separated in the original feature space using t-SNE (**Supplementary Fig. 3d**). After adding the SE module and residual block processing, the t-SNE clustering performance on the positive and negative samples could be significantly improved, thus leading to the apparent discriminative power of the final output from the fully connected layers (**Supplementary Fig. 3d**).

The classification performance of MuSIC's classifier was benchmarked against diverse machine learning and deep learning classifiers using the identical input features. We found that MuSIC consistently outperformed all the baseline classifiers, confirming the robustness and effectiveness of MuSIC in modeling RBP binding across species (**Supplementary Fig. 3e, f**).

MuSIC outperforms existing computational methods in predicting cross-species RBP–RNA interactions

We evaluated the prediction performance of MuSIC using 262 datasets from 186 RBPs, benchmarked under both within-species (224 datasets from 186 RBPs) and cross-species (38 datasets from 14 RBPs) scenarios (**Supplementary Table 3**). All the datasets were processed using a uniform preprocessing pipeline to ensure fairness in the performance evaluation (see **Methods** for details). Briefly, we performed a systematic comparison of prediction accuracy with four state-of-the-art computational methods, including HDRNet [31], PrismNet [30], DeepBind [28], and GraphProt [26]. As expected, MuSIC showed better prediction accuracy than other methods for the within-species prediction (AUC: MuSIC = 0.88, HDRNet = 0.87, PrismNet = 0.86, DeepBind = 0.67, GraphProt = 0.72) (**Supplementary Fig. 4a**).

We then evaluated the prediction accuracy of MuSIC and other computational methods in the cross-species prediction, where we trained the model in human and validated in mouse and zebrafish (19 datasets). MuSIC outperformed other methods, showing an obvious improvement of in AUC (AUC: MuSIC = 0.85, HDRNet = 0.73, PrismNet = 0.73, DeepBind = 0.71, GraphProt = 0.70; **Fig. 3a**), as well as in the Area Under the Precision-Recall Curve (PRAUC) and accuracy (ACC) metrics (**Supplementary Fig. 4b, c**). In addition, we found that MuSIC a significant performance improvement of AUC for predicting RBP–RNA interactions in the closely related predictions, e.g., trained in human and validated in mouse (**Supplementary Fig. 4d-f**). For example, MuSIC showed AUCs of 0.88 for YTHDC2 and 0.89 for TAF15 in the cross-species prediction, a significant improvement than other computational methods (**Fig. 3b** and **Supplementary Fig. 5a**). Taken together, these results showed that MuSIC could improve the prediction accuracy of RBP–RNA interactions than other computational methods, especially under the cross-species scenario. Consistently, MuSIC showed better performance in separating the positive and negative samples of input RNA sequences in the feature space than other computational methods (**Fig. 3c** and **Supplementary Fig. 5b**).

Finally, we compared the prediction accuracy of MuSIC and other computational methods by evaluating to what degree the RBP-binding peaks from CLIP-seq experiments could be rediscovered (see **Methods** for details). Briefly, the model was trained based on the RBP-binding peaks in human, followed by predicting peaks across all the transcripts in mouse (for 22 RBPs) and zebrafish (for 1 RBP) (**Supplementary Table 4**). For each RBP, we observed that MuSIC showed consistently better performance than other computational methods (**Fig. 3d**), particularly on the cases of AGO2, SRRM4, and Hnrnpa1 (**Fig. 3e**). Notably, HDRNet was excluded in this analysis due to its reliance on the experimental RNA structure features, which were not available in the relevant mouse datasets. For all the 23 RBPs analyzed here, the predicted peaks by MuSIC showed high correlation with the experimentally derived ones ($r = 0.73$, Spearman's rank correlation test; **Supplementary Fig. 6a-c**). Here, we showcased the site-level prediction performance of MuSIC using SRSF3 within the local genomic region (chr7: 96,200,000–96,400,000) in mouse, where 13 out of 17 experimentally derived peaks could be successfully recovered by MuSIC (**Fig. 3f**). In contrast, only 4 peaks could be predicted by other computational methods. These findings confirm the feasibility and effectiveness of MuSIC in accurately capturing RBP–RNA interactions across species.

MuSIC generates systematic RBP-binding predictions in diverse species

The aforementioned results reveal that MuSIC could generate better cross-species predictions than other computational methods, particularly when the source and target species are more evolutionarily closed. It will be useful to explore to what degree the source and target species are evolutionarily closed, then the MuSIC can generate reliable prediction results. We then evaluated the relationship between the prediction accuracy and the RBP conservation between species in terms of both their sequence and structure (**Supplementary Fig. 7a**; see **Methods** for details). Notably, we observed a strong positive correlation ($r = 0.76$, Pearson's correlation test; Fig. 4a) between the prediction accuracy (measured by AUC) and the RBP conservation based on 14 RBPs shared between mouse and zebrafish, indicating that the degree of RBP conservation could be used to quantificationally threshold the prediction results of RBP–RNA interactions. We then predicted the RBP–RNA interactions for the 10 species in a broad evolutionary range using MuSIC, and filtered low-confidence prediction results based on the degree of RBP conservation equivalent to AUC of 0.8 (see Methods for details).

As expected, more than 90% of the RBPs showed high-confidence prediction results (i.e., with prediction AUC > 0.8) in the species closely related to human, including orangutan, monkey, mouse and rat (Supplementary Fig. 7b). In contrast, only a small fraction (32.9%–68.1%) of the RBPs showed high-confidence prediction results in the remaining distantly related species, such as yeast, *A. thaliana* and fly (Supplementary Fig. 7b). Taken together, these findings confirm that MuSIC performs significantly better in the closely related species, by leveraging the RBP conservation patterns in terms of both sequence and structure (Supplementary Fig. 7b and Supplementary Table 5).

MuSIC improves RBP-binding motif identification in diverse species

Previous studies have revealed that conserved RBPs tend to have conserved RBP-binding motifs during evolution, which has been validated by some specific RBPs [41,42]. However, this hypothesis has not been systematically tested in a broad set of RBPs. To this end, we first predicted the RBP-binding peaks across all the 11 species using the trained 2,046 RBP models, and identified the enriched RBP-binding motifs in the human and non-human species (Supplementary Table 5). The predicted enriched motifs in the non-human species could be successfully recapitulated by the well-known RBP binding sequence preference [48]. For example, the motif CAUCU for YBX3, GGA for SRSF1 and polyC for KHSRP could be rediscovered in mouse, rat and chicken, respectively (Fig. 4b and Supplementary Fig. 7c). We then generated a catalog of RBP-binding motifs in all the 11 species ranging from human to yeast, and visualized the motif clustering based on their similarities (Fig. 4c; see Methods for details). Notably, RBP-binding motif prediction failed for certain RBPs due to their weak or undetectable binding signals in the distantly related species, such as yeast, fly, and zebrafish.

The inferred RBP-binding motifs with high confidence showed distinct degree of conservation during evolution (**Supplementary Fig. 7d** and **8**, **Supplementary Table 5**). For example, HNRNPA1 was predicted to contain GA-rich (e.g., GAA/AG) motifs in the closely related species (e.g., orangutan, monkey, and mouse) (**Supplementary Fig. 7d**). In contrast, the UGUANA-like motifs for PUM2 could be predicted in diverse species ranging from human to yeast (**Supplementary Fig. 7d**), consistent with the well-known motif UGUANAUA for PUM2 across multiple species [51]. Overall, the predicted RBP-binding peaks by MuSIC enables the identification of RBP-binding motifs in diverse non-human species, revealing the conserved and diverged binding preference of specific RBPs.

MuSIC reveals evolutionarily conserved RBP-binding peaks

It has been shown that the RBP-binding peaks from an RBP are either evolutionarily conserved or species-specific [43,52]. The conservation patterns of RBP-binding peaks could be influenced by both the RBP itself and the conservation of the target RNA sequence. To systematically evaluate the conservation of RBP-binding across species, we analyzed the predicted RBP-binding peaks of 186 RBPs across 11 species in the conserved transcripts (**Supplementary Fig. 9a, b**; see **Methods** for details). As expected, we observed higher proportion of conserved RBP-binding peaks in the more closely related species (**Fig. 5a**). Almost 64% of the total RBPs analyzed here exhibited considerable global patterns of RBP-binding peaks conservation (**Fig. 5a**). We highlighted two RBPs, RBM15B and ALKBH1, with their RBP-binding peaks from 9 species on the evolutionarily conserved genomic region (**Fig. 5b**). Notably, there were fewer or none evolutionarily conserved RBP-binding peaks in the distantly related species.

We further investigated the conservation of RBP-binding peaks by analyzing the RBPs containing the same protein family from different species. The YTH family RBPs, which contain YTH protein domains, exhibited consistently strong RBP-binding peaks conservation across species (**Supplementary Fig. 9c**). In contrast, the CPSF family RBPs showed lower RBP-binding peaks conservation in the distantly related species (**Supplementary Fig. 9c**), consistent with previous studies reporting gradient conservation of the RBP-binding peaks [43]. Further exploration of the relationship between RBP-binding peaks conservation and species evolution revealed that, while CPSF family RBPs maintained the steady degree of RBP-binding peaks conservation of in mammals, an obviously decrease showed among the distantly related species (i.e., from frog; **Fig. 5c**). Similar patterns could be also observed in the YTH family RBPs (**Supplementary Fig. 9d**). Taken together, these results indicate that the RNA-binding domains may play critical roles in maintaining the conserved RBP-binding peaks across species.

MuSIC prioritizes genetic variation with consistent effects influencing RBP-binding across species

Genetic variations, such as SNVs, can potentially alter RBP-binding affinity by disrupting RNA target recognition, and thus cause functional abnormalities and severe diseases [8,53,54]. The ability of predicting RBP-binding peaks across species by MuSIC enables us to quantify and analyze the effects of SNVs on RBP binding in the homologous regions between human and non-human species, which will be valuable for leveraging model organisms such as mouse to interpret the RBP-mediated mechanisms of human disease-associated SNVs [10,55].

We first quantified and compared the binding affinity on the local regions with (i.e., alternative allele) and without (i.e., reference allele) SNVs using the eCLIP data [56] from 103 RBPs (**Supplementary Fig. 10a**; see **Methods** for details). We found that SNVs detected in CLIP data were relevant to modulating RBP-binding affinity (**Supplementary Table 6**). Inspired by these findings, we further evaluated the consistency between MuSIC predictions and experimental data for SNV effects. We found that MuSIC could accurately predict the RBP-binding affinity on the local region containing the reference and alternative alleles, which was exemplified with the cases of SRSF1 and DDX3X (**Fig. 6a, b** and **Supplementary Fig. 10b**; see **Methods** for details).

Next, we ask whether MuSIC could be applied in quantifying the effects of SNVs in the homologous regions between species (**Fig. 6c**; see **Methods** for details). By applying the analysis framework, we systematically screened the 32,207 synonymous SNVs in human genome, corresponding to 85,599 SNVs in the homologous regions in mouse genome. We predicted 59,811 SNVs in mouse genome that could potentially disrupt RBP binding (i.e., ΔSNV < -0.5) (**Fig. 6c**). Here, we showed an example: the SNV NC_000006.11: g.4059022A>G in the human transcript NM_003913.5 was predicted as disrupting PUM2 binding (ΔSNV = -0.898) (**Fig. 6d**), consistent with the predicted effect of the SNV located in the homologous mouse transcript ENSMUST00000220965.2 (ΔSNV = -0.805) (**Fig. 6e**). Furthermore, we performed RNA pull-down *in vitro* and POND-qPCR [57] *in vivo* assays to validate the predictions by MuSIC. The POND (**P**rotein nanocage-emp**O**wered **N**on-**D**estructive) method is a recently developed novel technique for *in vivo* detection of RBP–RNA interactions, which enables selective packaging of RBP–RNA complexes into extracellular nanovesicles [57] (**Supplementary Fig. 11a**). We focused on three SNVs predicted by MuSIC showing disrupted binding affinity by PUM2 in both human and mouse (**Supplementary Table 7**). The RNA pull-down *in vitro* results confirmed that the alternative allele could indeed significantly impact PUM2 binding on the target RNA sequences in human and mouse (**Fig. 6f** and **Supplementary Fig. 11b, c**). In addition, the POND-qPCR *in vivo* results also supported these observations in human and mouse (**Fig. 6g**), confirming that MuSIC can generate accurate and reliable prediction on the effects of homologous SNVs on RBP binding across species.

Pervasive influenced RBP-binding implicated in disease mechanisms

Among all the 186 RBPs analyzed for their binding affinity changes on the SNVs in mouse genome, 79 (42.5%) RBPs were found to be enriched with the biological processes associated with ubiquitination regulation and protein degradation (**Fig. 6h** and **Supplementary Fig. 12a, b**). Previous studies have revealed that ubiquitination-related processes are implicated in the pathogenesis of complex diseases, such as cancer [58–61] and neurodegenerative diseases [62–65], which can be also validated by the predictions by MuSIC (**Supplementary Fig. 12c**). These findings suggest the critical roles of SNVs in modulating RBP binding and influencing the ubiquitination-associated processes, which may be implicated in complex disease mechanisms through disrupting protein homeostasis.

In our analysis, TARDBP was prioritized as highly related to the ubiquitination-related processes. TARDBP has been reported to be critical in regulating protein homeostasis and protein folding, and abnormal TARDBP binding on the target RNA transcripts can lead to several diseases in human and mouse [66–70]. We confirmed that the SNV in mouse could disrupt TARDBP binding to *Usp25*, a gene involved in ubiquitin metabolism (**Supplementary Fig. 13a**). Moreover, the TARDBP-bound genes perturbed by SNVs were significantly enriched in the functions related to neural development, ubiquitination, deubiquitination, and protein metabolism (**Supplementary Fig. 13b, c**).

Discussion

Existing computational methods for predicting RBP–RNA interactions [26,28,30,31] were generally developed for the within-species tasks, having difficulties in predicting cross-species. In this study, we developed MuSIC, a novel computational method that can accurately predict RBP-binding peaks in the species lacking available CLIP datasets by leveraging the multi-level conservation patterns of the RBP. Compared to other similar computational methods, MuSIC showed superior performance in predicting RBP-binding peaks on the cross-species tasks. We then systematically predicted RBP-binding peaks and their enriched sequence motifs for 186 RBPs in human and 10 non-human species using MuSIC. We confirmed that the conservation patterns of the predicted RBP-binding peaks were consistent with previous studies [42,43,52]. Finally, we applied MuSIC to investigate the effects of SNVs on RBP binding, particularly focusing on the imbalance in RBP binding induced by SNVs and exploring their potential connections to diseases such as cancer and neurodegenerative disorders.

The following improvements in the model architecture are critical for the augmented prediction performance of MuSIC in the cross-species tasks: optimization of input feature length and label smoothing. Previous studies have showed that increasing input sequence length can dramatically improve the model performance [24,71]. In our study, we revealed that increasing the input sequence length from 101nt to 200nt could significantly improve the prediction performance across species (AUC from 0.55 to 0.75). In contrast, increasing the input sequence length from 200nt to 400nt would lead to decreased model performance. Increasing the input sequence length can not only provide more useful sequence information, but also may include noisy and redundant sequence information for modeling RBP binding. Inspired by the concepts from computer vision, we implemented label smoothing in the model to further improve prediction performance [35–37]. We showed that label smoothing and the gradient weight adaptation mechanism could significantly improve cross-species predictions. This strategy reflects the inherently dynamic nature of biomolecular recognition, which operates on a continuum rather than a binary decision framework [72].

The MuSIC model exhibited lower prediction confidence in the distantly related species, such as fly, *A. thaliana* and yeast, partially due to the decreased evolutionary conservation of RBPs in these species. With the advancement in large language models, RBP-guided RNA generation strategies could increase the prediction confidence of RBP-binding peaks in distantly related species [73]. For example, BERT-RBP [74] was developed by adapting the pretrained BERT architecture and leveraging long-range RNA sequence features in predicting RNA-RBP interactions with improved performance. Similarly, ZHMolGraph [75] was proposed to predict novel RBP–RNA interactions by combining graph neural networks with unsupervised large language models. In the future, we hope that incorporating large language model-based diffusion methods into the MuSIC model can improve the prediction performance by complementing the low conservation of RBPs in the distantly related species.

Previous studies revealed that genetic variation in RNA can potentially reduce RBP-binding affinity [8,53,76]. However, the effects of SNVs on RBP binding has not fully explored, particularly in the non-model organisms. In our study, we quantified the effects of SNVs on RBP binding in the homologous regions between human and mouse, and furthermore experimentally validated these prediction results *in vitro* and *in vivo*. Our results revealed the evolutionary conservation of genetic variation influencing RBP binding across species, and found that the SNVs that could potentially alter RBP–RNA interactions are associated with human diseases [9,10]. We then performed a comprehensive analysis on the homologous human SNVs in mouse to quantify their binding affinity changes for each of the 186 RBPs. Interestingly, the disrupted binding events generally are recognized by TARDBP, and the target transcripts are enriched with the ubiquitination-associated pathways [31]. The dysregulation of ubiquitin–proteasome system (UPS) can lead to protein misfolding and accumulation, which has been linked to human diseases including cancer and neurodegenerative disorders [65,77].

In summary, we propose MuSIC as a model to predict RBP-binding peaks across species. MuSIC outperformed state-of-the-art prediction models, and generated a catalog of predicted RBP-binding peaks of 186 RBPs with high accuracy in 11 species. The detailed analysis quantified the effects of genetic variants on RBP binding, particularly highlighted in the homologous regions between human and mouse. MuSIC provides insights into the RNA-RBP interactions in non-model organisms, and generates novel hypotheses on the interplays between RBP-mediated regulation and disease mechanisms.

Acknowledgements

We thank Chenqian Wang, Shaozhen Yin, Ruobin Zhao, Liangyu Li, Yongkang Tang and Suiru Lu for fruitful discussions and invaluable feedback. We thank Jindong Sun for running the software comparison benchmark. This work was supported by the National Natural Science Foundation of China (No.82341086, No.32300521, and No.32422013 to L.S., No.32025007 to Y.W.); the Open Grant from the Pingyuan Laboratory (No.2023PY-OP-0104 to L.S.); the State Key Laboratory of Microbial Technology Open Projects Fund (No.M2023-20 to L.S.); the Intramural Joint Program Fund of the State Key Laboratory of Microbial Technology (NO.SKLMTIJP-2024-02 to L.S., and T.Z.); the Shandong Province Postdoctoral Innovation Project (NO. SDCX-ZG-202400146 to T.Z.), the Qingdao Postdoctoral Science Foundation (NO. QDBSH20240102200 to T.Z.), the Double-First Class Initiative of Shandong University School of Life Sciences; the Young Innovation Team of Shandong Higher Education Institutions, the Taishan Scholars Youth Expert Program of Shandong Province, and the Program of Shandong University Qilu Young Scholars.

Author’s Contribution

L.S. conceived the project. L.S., Y.T.Y. and Y.W. supervised the project. J.H., and T.Z. established the initial technical framework. J.H. performed the computational analyses, data curation, and methods development. J.H., Q.C., S.Y. and W.Z. trained the deep learning models. L.H. and Y.W. conducted *in vivo* and *in vitro* experimental design and validation. Y.J., T.Z. and S.J. collected and re-analyzed the RBP similarity data. J.H. and J.W. collected and re-analyzed RBP-binding peaks data based on CLIP-seq. J.H., T.Z., and W.Z. deployed and tested the availability of the MuSIC scripts. J.H. and T.Z. written the initial draft of the manuscript. Y.T.Y., L.H., Q.C., J.Z., M.J., Y.L. and X.W. providing critical feedback and suggestions for improvement. J.H. formatted the figures, and L.S. and Y.T.Y. prepared the final version of the manuscript.

Availability of data and materials

An implementation of the MuSIC script and benchmarking data is available at https://github.com/GALE1228/MuSIC_pretrain.

Ethics approval and consent to participate

Not applicable.

Consent for publication

Not applicable.

Competing interests

The authors declare that they have no competing interests.

Methods

Compiling RBP-binding peak datasets

We obtained the RBP-binding peaks of 216 RBPs from POSTAR3 [32] for the within- and cross-species model training and testing. We applied a uniform preprocessing pipeline to the peak datasets to minimize putative bias in the datasets. Briefly, we first removed the duplicated and short (length < 5nt) peaks in each dataset. Then, we selected the top 5000 peaks with the highest binding strength in each dataset for the downstream analysis. Next, the peaks were extended by 200nt on both sides. We used GFF Annotation Parser (https://github.com/lipan6461188/GAP) to extract the RNA sequences of these extended peaks, which were considered as the positive peaks (i.e., RBP-binding peaks) in the model training and validation. We randomly selected 5000 RNA sequences of 200nt in length from the remaining genomics regions as the negative ones.

For the within-species prediction, 224 datasets of 186 RBPs from human, mouse, and zebrafish were used. For the cross-species prediction, 17 datasets of 13 RBPs shared between human and mouse, and 2 datasets of one RBP shared between human and zebrafish were used. Notably, the datasets of the same RBP generated by different CLIP-seq technologies were excluded in the cross-species analysis. For the within-species prediction, we used randomly 80% of the positive and negative peaks for the model training, whereas 20% were used for the model validation. For the cross-species prediction, we simply maintained a training-to-validation ratio of 4:1 by randomly selecting the positive and negative peaks from the source and target species.

Reconstructing phylogenetic tree among the 11 species

We aim to develop a novel computational method to systematically predict RBP–RNA interactions in 11 species, including *Homo sapiens* (human), *Pongo abelii* (orangutan), *Macaca fascicularis* (monkey), *Mus musculus*(mouse), *Rattus norvegicus* (rat), *Gallus gallus* (chicken), *Xenopus laevis* (frog), *Danio rerio* (zebrafish), *Drosophila melanogaster* (fly), *Arabidopsis thaliana* (*A. thaliana*), and *Saccharomyces cerevisiae* (yeast).

We retrieved the 18S rRNA sequences of the 11 species from RNAcentral [78] (Release 24) for evaluating the evolutionary distance among these species. We then performed multiple sequence alignment of the 18S rRNA sequences using the Sequence Alignment tool in MEGA [79] v11.0.13, followed by constructing a phylogenetic tree among the 11 species using the neighbor-joining method. We then evaluated the reliability of the reconstructed phylogenetic tree using the Bootstrap test with 1000 replicates.

Compiling sequence and structural datasets of RBPs

We collected the protein IDs of 216 RBPs [32] that were used in this study in the 11 species from UniProt [51] (**Supplementary Table 1**). For each RBP, the corresponding sequences and structural data were retrieved from UniProt [51]. In the cases where predicted structural data for certain RBPs were unavailable in UniProt, we used AlphaFold2 [80] to predict and supplement the missing ones. The sequence similarity of the full-length RBPs between human and other species was computed using ClustalX [81] v2.1.1. We used US-align [82] to evaluate the structural similarity of the full-length RBPs by calculating two metrics: TM-score (overall structure similarity) and pLDDT (confidence of predicted structure).

We obtained the annotations of 130 RBDs in the 11 species from InterPro [83] (Release 103.0), including their sequence positions and respective fragments in their full-length RBPs. The local structures of RBDs were extracted from the structures of full-length RBPs, ensuring the local structures of RBDs were aligned with the structures of full-length RBPs. Finally, ClustalX [81] v2.1.1 and US-align [82] were used to calculate the sequence and structural similarity of the RBDs between human and other species.

Comparing RBP–RNA interactions in three-dimensional structures between species

We collected three-dimensional structures of homologous RBP RC3H1 (PDB ID 4QIL in human, PDB ID 4QI2 in mouse) and their bound RNA fragments from the PDB [84]. In addition, we used AlphaFold3 [49] webserver to predict the interactions between homologous RBP IGF2BP1 and bound RNA fragments in human and mouse based on the IGF2BP1 protein sequence in human and mouse, as well as well-known RNA sequence with strong preference by IGF2BP1 (5'-UGACUUACUUCAUUAUUGAA-3'). The cartoon and surface diagrams displaying the bound RNA, RBDs, and the residues involved in the interactions were generated using PyMOL v3.1.0 (http://www.pymol.org/pymol).

Pre-processing MuSIC input data

The RNA sequence of each peak in the datasets was first transformed into a one-hot encoded matrix of size (4, 200), where the four rows correspond to the nucleotides A, C, G, and U. The secondary structure of each RNA sequence was predicted using RNAfold [85] v2.1.0 with default settings. The resulting structure was encoded into a 2-dimensional matrix of size (2, 200), with 'P' and 'U' representing the paired and unpaired bases, respectively. The sequence and structure matrices were then concatenated along the channel axis to generate a unified (6, 200) representation encoding both sequence and structural features, which will be used as the input data for the MuSIC model.

Overview of MuSIC architecture

The input data for MuSIC is defined as *S*, which contains *N* peaks. Each sample, $s \in S$, is an RNA sequence of length *L* = 200nt. As described above, *s* corresponds to a sequence-and-structure vector of D = 6 dimensions. Therefore, *S* is encoded into a tensor $X \in R^{N\times \mathrm{D}\times \mathrm{L}}$ and the binding probability $Y \in R^{N}$ is computed by as follows:

$$Y = \text{MuSIC}(X)$$

MuSIC is defined as follows:

$$\text{MuSIC}(X) = \sigma(\,\mathrm{FC}(f_R(f_S(f_C(\mathrm{X})))))$$

where σ is the sigmoid activation function, FC is the fully connected layer, f_R is the residual blocks, f_S is the squeeze-excitation block (SE), and f_C is the convolutional block, respectively.

Convolutional Block

First, we use a convolutional layer to extract features. The convolutional block $f_C(X)$ is defined as follows:

$$f_C(X) = \text{ReLU}\left(\text{BN}\left(\text{Conv}_{K,P}(X)\right)\right)$$

where $\text{Conv}_{K,P}(X)$ is a 2D convolutional layer with kernel K and padding P. The convolutional layer is designed to extract local sequence and structural features from the input data.

Squeeze-and-Excitation (SE) Block

We apply a Squeeze-and-Excitation (SE) block to recalibrate channel-wise feature responses. The SE block is defined as follows:

$$f_S(X) = X \otimes \text{SE}(X)$$

$$\text{SE}(X) = \sigma\left(f_{\text{ex}}\left(f_{sq}(X)\right)\right)$$

where σ is the activation function, f_{sq} is a global average pooling function to squeezes the global sequence and structural features into a channel statistic and f_{ex} applies a nonlinear transformation to the squeezed feature map. The SE block helps the model focus on the most relevant features for RBP binding.

Residual Blocks

We then use residual blocks to capture both sequence and structural features over long ranges. These residual blocks are designed to learn the hierarchical features by passing information through several convolutional layers. Two types of residual blocks are used here:

ResidualBlock2D, which operates on 2D feature maps, is defined as follows:

$$f_R(X) = \text{ResidualBlock2D}\left(\text{Conv}\left(\text{SE}(X)\right)\right)$$

ResidualBlock1D, which operates on 1D feature maps, is defined as follows:

$$f_R(X) = \mathrm{ResidualBlock1D}\left(\mathrm{AvgPool}\left(\mathrm{ResidualBlock2D}(X)\right)\right)$$

Fully Connected Layer

Finally, we apply a fully connected layer to generate the binding probability prediction for each RNA input sequence, which is defined as follows:

$$Y = \sigma\left(f_{\mathrm{FC}}(x)\right)$$

Label smoothing strategy and gradient weight adaptation

We applied the label smoothing strategy to smooth the one-hot label distribution. Given a one-hot label vector $q(x)$, the smoothed label distribution $q'(x)$ is defined as follows:

$$q'(x) = \alpha q(x) + (1 - \alpha)u(x)$$

where α is the RBP conservation score as a smoothing coefficient, and $u(x)$ is the uniform distribution.

The one-hot label distribution $q(x)$ and a predicted binding probability distribution $p(x)$ are used for computing the classification loss as follows:

$$L_{ture} = \mathcal{H}\left(q(x), p(x)\right) = -\sum_{i=1}^{C} q\,(x_i)\log\left(p(x_i)\right)$$

The smoothed label distribution $q'(x)$ and a predicted binding probability distribution $p(x)$ are used for computing the smoothing loss as follows:

$$L_{smooth} = \mathcal{H}\left(q'(x), p(x)\right) = -\sum_{i=1}^{C} q\,'(x_i)\log\left(p(x_i)\right)$$

$$L_{smooth} = \mathcal{H}\left(q'(x), p(x)\right) = -\sum_{i=1}^{C} \alpha q(x_i)\log\left(p(x_i)\right) - \sum_{i=1}^{C}(1 - \alpha)u(x_i)\log\left(p(x_i)\right)$$

The first term, L_{true}, represents the typical classification loss, while the second term, L_{smooth}, is the smoothing loss. Finally, the total loss is defined as the weighted combination of classification loss and smoothing loss as follows:

$$L_{total} = \alpha L_{ture} + \beta L_{smooth}$$

We proposed gradient weight adaptation to address the conflict between the gradient directions of L_{ture} and L_{smooth}. First, the gradients of both losses are computed with respect to the feature encoder parameters and classifier parameters as follows:

$$\nabla L_{ture\text{(encoder)}} = \frac{\partial L_{ture}}{\partial \theta_{\text{encoder}}}, \quad \nabla L_{smooth\text{(encoder)}} = \frac{\partial L_{smooth}}{\partial \theta_{\text{encoder}}}$$

$$\nabla L_{ture(\mathrm{classifier})} = \frac{\partial L_{ture}}{\partial \theta_{\mathrm{classifier}}}, \quad \nabla L_{smooth(\mathrm{classifier})} = \frac{\partial L_{smooth}}{\partial \theta_{\mathrm{classifier}}}$$

The weight of each loss term can be dynamically adjusted based on the ratio of the current loss to the previous one as follows:

$$\Delta_{ture} = \frac{L_{ture}}{L_{ture}^{t-1}}, \quad \Delta_{smooth} = \frac{L_{smooth}}{L_{smooth}^{t-1}}$$

$$w_{smooth} = \frac{1}{\Delta_{smooth}}, \quad w_{ture} = \frac{1}{\Delta_{\text{true}}}$$

$$w_{smooth} = \frac{w_{smooth}}{w_{smooth} + w_{ture}}, \quad w_{ture} = \frac{w_{\text{cls}}}{w_{smooth} + w_{ture}}$$

Subsequently, the gradient can be expressed as follows:

$$\nabla L_{\text{total(encoder)}} = w_{smooth} \nabla L_{smooth\text{(encoder)}} + w_{ture} \nabla L_{ture\text{(encoder)}}$$

$$\nabla L_{\text{total(classifier)}} = w_{smooth} \nabla L_{smooth(\mathrm{classifier})} + w_{ture} \nabla L_{ture(\mathrm{classifier})}$$

By dynamically adjusting w_{ture} and w_{smooth}, the model can effectively prioritize the loss terms that show significant changes in the optimization process

MuSIC model training

We applied the label smoothing strategy to smooth the one-hot label distribution and calculated the total loss as described above. The gradient weight adaptation dynamically modulated relative weights between L_{ture} and L_{smooth} according to the ratio of the current loss to the previous one, ensuring efficient gradient propagation.

The parameters in MuSIC model were optimized by minimizing the total loss—this loss integrates the classification loss and the smoothed label loss. We used Adam to optimize the model parameters, and Gradual Warmup Scheduler to adjust the learning rates. Throughout model training, we periodically evaluated the prediction performance of the model on the validation set to find the optimized parameters for the model.

MuSIC hyperparameter settings

The hyperparameters of MuSIC were empirically adjusted based on the cross-species datasets. The hyperparameter settings for MuSIC are defined as follows:

Convolutional layer: the convolutional layer uses a kernel size of (3, 3) with 16 output channels, followed by Batch Normalization (BN) and ReLU activation for non-linearity.

Pooling layer: average pooling is applied with a kernel size of (6, 1), which reduces the feature map along the first axis of the input tensor.

Full connection layer: the fully connected layer at the end of the network has 1 output unit, which corresponds to the predicted binding probability for each sample.

Dropout probability: dropout is applied with probabilities of 0.1, 0.5, and 0.3 at different layers in the network to prevent overfitting.

L2 norm penalty: the L2 norm penalty (weight decay) is set to 1×10^{-6}, which applies regularization to the model's weights during optimization.

Batch size: the batch size is set to 64 for training and evaluation.

Learning rate: the learning rate is set to 0.001 for the Adam optimizer, which is used to optimize the network's parameters.

Positive weight in loss function: the positive weight in the loss function is set to 2, which accounts for class imbalance in the dataset, giving more importance to positive samples during training.

Training epochs: the number of training epochs is set to 200, which determines how many times the model will iterate over the entire training dataset.

Early stop: early stopping is applied with a patience of 20 epochs, meaning training will halt if the model's performance does not improve on the validation set for 20 consecutive epochs.

Initial weights: the initial weights of the model are set using the Kaiming normal initialization for convolutional layers and Xavier initialization for fully connected layers.

Ablation experiments of MuSIC model

We performed the ablation experiments to explore to what degree the features could enhance the model performance: (i) input sequence length: we tried different input sequence lengths of 101nt, 200nt and 400nt; (ii) label smoothing strategy: we added and removed the label smoothing strategy in the models; (iii) sequence and structural features: we constructed the models using different types of input data, including only sequences, only predicted structures, combined sequences and predicted structures, and combined sequences and experimentally-measured structures.

Performance comparison with other computational methods

We compared the prediction performance of MuSIC with other recently published computational methods, including HDRNet (https://github.com/zhuhr213/HDRNet) [31], PrismNet (https://github.com/kuixu/PrismNet) [30], DeepBind (https://github.com/jisraeli/DeepBind) [28], and GraphProt (https://github.com/dmaticzka/GraphProt) [26]. Notably, to make a fair comparison, each of these computational methods was trained and validated on the same datasets as used in MuSIC, using their default parameter settings.

We extracted the features from the fully connected layers of MuSIC and the other four computational methods, including HDRNet [31], PrismNet [30], DeepBind [28], and GraphProt [26]. These features were projected into a two-dimensional space using t-SNE to visualize and compare their classification performance.

We used MuSIC and the other four computational methods to train cross-species models and predict RBP-binding peaks for 22 RBPs from mouse and one RBP from zebrafish. We then estimated the prediction performance of the computational methods based on the overlap between the predicted peaks with binding probabilities above 0.9 and the experimentally-derived peaks. We also calculated the correlation between the predicted peaks and experimentally-derived peaks as we did in the meta-transcript analysis mentioned above.

Thresholding high-confidence RBP across species predicted by MuSIC

We considered the six RBP features for RBP conservation analysis, including the full-length sequence similarity, the full-length structural TM-score, the full-length structural pLDDT, the RBD sequence similarity, the RBD structural TM-score, and the RBD structural pLDDT. We then applied Principal Component Analysis (PCA) to calculate the first principal component (PC1) as RBP conservation.

We then analyzed the correlation between the RBP conservation scores and the AUC scores of 14 RBPs derived from the cross-species analysis. We observed a linear correlation and constructed a regression model between the two variables, which can be used for estimating the cross-species prediction accuracy (i.e., AUC score) of the peaks (**Supplementary Table 4**). We applied a threshold of 0.8 for the AUC scores to retain the high-confidence predicted peaks.

Identifying and clustering RBP-binding motifs

A total of 2046 models for predicting RBP–RNA interactions in 11 species were trained using 186 high-quality peak datasets from human [32]. RNA sequences from each species were segmented into the fragments of 200nt in length, and 20,000 fragments were randomly sampled for further analysis. In each species, each of the MuSIC models of the 186 RBPs generated predicted peaks on these fragments. We then applied MEME [86] v5.5.7 to identify the enriched RBP-binding motifs using the fragments with binding probabilities above 0.9.

We performed motif clustering in two steps. First, for each motif, we calculated base frequency by averaging the nucleotide frequencies (A, C, G, U) from its position weight matrix (PWM) as follows:

$$\text{Base Frequencies}_i = (A_i, C_i, G_i, U_i)$$

where A_i, C_i, G_i, U_i are the average frequencies of adenine (A), cytosine (C), guanine (G), and uracil (U) for the motif i, respectively.

Second, we calculated the similarity matrix by integrating the Jensen–Shannon (JS) divergence of PWM distributions and the Euclidean distance between base frequency vectors:

$$S_{ij} = \alpha \cdot JS(i,j) + (1-\alpha) \cdot d_{\text{euclid}}(i,j)$$

$$JS(i,j) = \frac{1}{8}\sum_{k=1}^{8} \text{Jensen-Shannon}\left(\text{PWM}_i[k], \text{PWM}_j[k]\right)$$

$$d_{\text{euclid}}(i,j) = \sqrt{\left(A_i - A_j\right)^2 + \left(C_i - C_j\right)^2 + \left(G_i - G_j\right)^2 + \left(U_i - U_j\right)^2}$$

where $\text{PWM}_i[k]$ is the k-th row of the PWM matrix for motif i, $\text{PWM}_j[k]$ is the k-th row of the PWM matrix for motif i, $d_{\text{euclid}}(i,j)$ is the Euclidean distance between the base frequency vectors of motif i and j, α is a hyperparameter balancing the weight of the JS divergence and Euclidean distance.

Finally, we grouped the motifs using hierarchical clustering to show their overall similarity. We used the itol.toolkit package [87] v1.1.10 to visualize and map the motif logo to the clustering results.

Analyzing conservation patterns of RBP-binding peaks predicted by MuSIC

Using human transcripts as the reference, we applied the Mashmap [88] v3.1.3 to compare pairwise species (i.e., human and non-human species) and select the highest conserved transcripts with segment length > 500nt. For each species, MuSIC was used to predict RBP-binding peaks with 200nt and high attention regions [30] with 40nt for 186 RBPs in these conserved transcripts.

The conserved transcripts from 11 species were subjected to multi-sequence alignment by using Muscle5 [89] v5.1 with default parameters, and high attention region coordinates were aligned accordingly. RBP-binding peaks overlap counts across species were statistically analyzed within an extended window of 200nt. We then used IGV [90] v2.16.2 to visualize the RBP-binding peaks in the conserved transcripts from 11 species.

Evaluating consistency between MuSIC predictions and experimental data for SNV effects

We downloaded the eCLIP peaks of 103 RBPs in HepG2 cell line from ENCODE (https://www.encodeproject.org/publication-data/ENCSR456FVU/). The SNVs in the RBP-binding peaks of each RBP were then identified from the eCLIP mapping files (i.e., BAM files) using the BCFtools mpileup [91] v1.20, where the replicates were merged. Peaks regions were filtered ($p.adj \leq 0.05$) and merged across three replicates to retain high-confidence RBP-binding peaks. Using BEDTools [92] v2.27.1 , SNV positions were overlapped with peak regions to classify peaks into SNV-overlapping and non-overlapping groups. A paired t-test was then applied to compare signal differences between the two groups.

We analyzed the RNA-seq alignment files from the smartSHAPE datasets (GSE145805) to estimate the background allele ratio. For both eCLIP and RNA-seq datasets, we calculated their reference allele (REF) and alternative allele (ALT) ratios using BCFtools mpileup [91] v1.20, and then obtained $diff_{ratio}$, the difference between the REF and ALT ratios from the RNA-seq and eCLIP datasets as follows:

$$diff_{ratio} = \frac{eCLIP_{ALTratio}}{RNAseq_{ALTratio}} - \frac{eCLIP_{REFratio}}{RNAseq_{REFratio}}$$

In parallel, we also calculated $diff_{score}$, the predicted difference between the REF and ALT ratios as follows:

$$diff_{score} = Pred_{ALT} - Pred_{REF}$$

where $Pred_{ALT}$ and $Pred_{REF}$ are predicted binding possibilities for the sequences containing the ALT and REF, respectively.

We pre-processed the SNV effects by retaining $|diff_{ratio}| \geqslant 0.2$ and $|diff_{score}| \geqslant 0.2$, and then extracting the top 80% ranked by $diff_{score}$. We used the experimental labels ($label_{exp}$) and the predicted labels ($label_{pre}$) to evaluate the consistency between experimental data and MuSIC predictions for SNV effects. The $label_{exp}$ and $label_{pre}$ are defined as follows:

$$label_{exp} = 1 \text{ when } diff_{ratio} \geqslant 0;\ label_{exp} = 0 \text{ when } diff_{ratio} < 0$$

$$label_{pre} = 1 \text{ when } diff_{score} \geqslant 0;\ label_{pre} = 0 \text{ when } diff_{score} < 0$$

The consistency between $label_{exp}$ and $label_{pre}$ was evaluated using Fisher's exact test, with multiple testing corrected by the Benjamini–Hochberg method, and results with FDR ≤ 0.05 were considered statistical significance.

Quantifying the effects of homologous SNVs between human and mouse on RBP-binding using MuSIC

We downloaded the human and mouse RNA sequences from Ensembl [93] (Release 113). We extracted the human RNA sequences overlapping with the nonsense SNV positions from dbSNP [6] using the GAP (https://github.com/lipan6461188/GAP), and then generated the two sequences containing the REF and ALT for each SNV. We then identified the homologous regions of the human SNV-containing sequences in the mouse genome using BLAST [94] v2.16.0. In total, 32,207 nonsense SNVs in human, and 85,599 homologous nonsense SNVs in mouse were included for further analyses.

We then used MuSIC to predict the binding possibilities on the RNA sequences containing the REF and ALT in human and mouse for each of the 186 RBPs. For each sequence, the effect of the SNV on RBP binding was defined as follows:

$$\Delta SNV = P_{ALT} - P_{REF}$$

where P_{REF} is the binding probability for the REF, P_{ALT} is the binding probability for the ALT.

Cell transfection

150,000 HEK293T cells per well were seeded in a well of poly-D-lysine-coated 24-well plates. After 16-20 h, cells were co-transfected with 200 ng EPN24-PUM2 plus 75ng GFP-REF or GFP-SNV target plasmid using JetPRIME reagent (Polyplus), the medium was refreshed at 4-6 h post-transfection, and the supernatant was collected for subsequent analysis 24 h after medium change.

RNA pull-down assay

The *in vitro* RNA pull-down assay was performed as described [95]. Briefly, 200 pmol biotinylated RNA oligonucleotides were refolded by heating at 90 °C for 1 min, and then incubated at 30 °C for 5 min. About 1×10^7 myc-PUM2-expressing HEK293T cells were lysed in 500 μl lysis buffer (150 mM NaCl, 1 mM EDTA, 1% Triton X-100, 0.5 mM

DTT, 50 mM Tris-HCl, pH 7.5, 0.5% sodium deoxycholate) with 5 μl PMSF (100mM, Beyotime), 10 μl phosphatase inhibitor cocktail (50 ×, Beyotime), 10 μl protease inhibitor cocktail (50 ×, Beyotime), 2.5 μl SUPERase In inhibitor (20U/μl Invitrogen) and 5 μl RNase Inhibitor (40U/μl, Beyotime). Refolded RNA (8 μl) and 500 μl cell lysate were incubated at 4 °C for 3-4 h. Then 100 μl pre-washed VAHTS CA-28 Streptavidin Beads (Vazyme) were added into the buffer and incubated at 4 °C for 1h. The beads were washed first with high salt buffer (50 mM Tris-HCl, pH 7.5, 1 M NaCl, 1% TRITON X-100) at room temperature for 5 min and then 2 more times with low salt buffer (50 mM Tris-HCl, pH 7.5, 150mM NaCl, 1% TRITON X-100), at room temperature and for 5 min. Proteins were eluted in 50 μl 1× SDS-PAGE loading buffer (Beyotime) at 98 °C for 20 min.

Protein electrophoresis was performed using BeyoGel™ Elite Precast PAGE Gel (8-16%, Beyotime), followed by protein transfer onto polyvinylidene fluoride (PVDF) membrane. The Myc Tag Mouse Monoclonal Antibody (HRP Conjugated) (Beyotime, AF2867) were diluted (1:1000) and incubated with the membrane at 4°C overnight. After three washes with 1×TBST buffer, the membrane was treated with electrochemiluminescence (ECL) reagent (Merck Millipore, WBKLS0050) and imaged with eBLOT14 Touch Imager (e-BLOT).

POND-qPCR

Cell supernatant was clarified by centrifugation at 3,000 g for 5 minutes, then filtrated through a cellulose acetate filter with 0.45 μm pore size (Corning). 200 μl of supernatant was mixed with 800 μl TRIzol reagent (Magen) and 1 μl diluted External RNA Controls Consortium (ERCC, 1:1000) synthetic spike-in RNAs (ThermoFisher). RNA was extracted and dissolved in 20 μl nuclease-free water.

Next, 3 μl of supernatant RNAs or 250 ng cellular total RNA were reverse transcribed using HiScript® III RT Super Mix (Vazyme) at 37°C for 15 minutes. The cDNA products were diluted five-fold with 20 μl nuclease-free water, and 1 μl aliquot was used for real-time qPCR with AceQ qPCR SYBR Green Master Mix (Vazyme) in

96-well plates on the StepOne Plus Real-Time PCR System (Applied Biosystems) following standard protocols.

Large-scale screening of RBPs affected by SNVs in UPS

For each RBP, SNVs with strong effects were identified: ΔSNV < -0.2 and P_{WT} > 0.6. We annotated the transcripts affected by SNVs using the GAP (https://github.com/lipan6461188/GAP).

We used the STRING [96] database (https://string-db.org/) to annotate the enriched biological functions of SNV-affected transcripts. Among the top five enriched biological functions, we selected those related to ubiquitination or deubiquitination. Then, we categorized the RBPs into four groups according to the functional enrichment with ubiquitination or deubiquitination for their target transcripts affected by SNVs, i.e., the highly ubiquitin-related (both ubiquitination- and deubiquitination-related), the weakly ubiquitin-related (either ubiquitination- or deubiquitination-related), the not ubiquitin-related (not ubiquitination- or deubiquitination-related), and the not function-enriched.

We then performed the KEGG enrichment analysis on the SNV-affected transcripts annotated with highly ubiquitin-related. The enriched disease pathways revealed potential regulatory associations among SNVs, RBPs, and disease-relevant UPS genes.

Quantification and statistical analysis

All statistical analyses were performed with R. Where applicable, the sample size (N) was specified either in the plot or in the corresponding figure legends. Analysis details could be found in the method section, such as statistical tests, definitions, etc. Boxplots were used to visualize the distribution of the data, with the box representing the interquartile range (IQR). The median was indicated by a horizontal line within the box, while the upper and lower hinges represented the 75th and 25th percentiles, respectively. The whiskers extended to the most extreme data points within 1.5 times the IQR from the box. Any data points beyond this range were considered outliers and plotted individually. Statistical significance was determined using appropriate tests, with *P* reported in the figure legends or main text.

References

1. Castello, A. *et al.* Insights into RNA Biology from an Atlas of Mammalian mRNA-Binding Proteins. *Cell* **149**, 1393–1406 (2012).
2. Gerstberger, S., Hafner, M. & Tuschl, T. A census of human RNA-binding proteins. *Nat Rev Genet* **15**, 829–845 (2014).
3. Corley, M., Burns, M. C. & Yeo, G. W. How RNA-Binding Proteins Interact with RNA: Molecules and Mechanisms. *Molecular Cell* **78**, 9–29 (2020).
4. Li, Y. & Sun, S. RNA dysregulation in neurodegenerative diseases. *EMBO J* **44**, 613–638 (2025).
5. Gebauer, F., Schwarzl, T., Valcárcel, J. & Hentze, M. W. RNA-binding proteins in human genetic disease. *Nat Rev Genet* **22**, 185–198 (2021).
6. Sherry, S. T. *et al.* dbSNP: the NCBI database of genetic variation. *Nucleic Acids Res* **29**, 308–311 (2001).
7. Landrum, M. J. *et al.* ClinVar: improving access to variant interpretations and supporting evidence. *Nucleic Acids Res* **46**, D1062–D1067 (2018).
8. Yang, E.-W. *et al.* Allele-specific binding of RNA-binding proteins reveals functional genetic variants in the RNA. *Nat Commun* **10**, 1338 (2019).
9. Van De Sompele, S. *et al.* Functional characterization of a novel non-coding mutation “Ghent +49A > G” in the iron-responsive element of L-ferritin causing hereditary hyperferritinaemia-cataract syndrome. *Sci Rep* **7**, 18025 (2017).
10. Yamazaki, T., Liu, L., Conlon, E. G. & Manley, J. L. Burkitt lymphoma-related *TCF3* mutations alter TCF3 alternative splicing by disrupting hnRNPH1 binding. *RNA Biology* **17**, 1383–1390 (2020).
11. Patton, E. E., Zon, L. I. & Langenau, D. M. Zebrafish disease models in drug discovery: from preclinical modelling to clinical trials. *Nat Rev Drug Discov* **20**, 611–628 (2021).
12. Choi, T.-Y., Choi, T.-I., Lee, Y.-R., Choe, S.-K. & Kim, C.-H. Zebrafish as an animal model for biomedical research. *Exp Mol Med* **53**, 310–317 (2021).
13. Liu, J. & Cao, X. RBP–RNA interactions in the control of autoimmunity and autoinflammation. *Cell Res* **33**, 97–115 (2023).
14. Bryant, C. D. & Yazdani, N. RNA -binding proteins, neural development and the addictions. *Genes Brain Behav* **15**, 169–186 (2016).

15. Ellington, A. D. & Szostak, J. W. In vitro selection of RNA molecules that bind specific ligands. *Nature* **346**, 818–822 (1990).
16. Ray, D. *et al.* Rapid and systematic analysis of the RNA recognition specificities of RNA-binding proteins. *Nat Biotechnol* **27**, 667–670 (2009).
17. Lambert, N. *et al.* RNA Bind-n-Seq: Quantitative Assessment of the Sequence and Structural Binding Specificity of RNA Binding Proteins. *Mol Cell* **54**, 887–900 (2014).
18. Gilbert, C. & Svejstrup, J. Q. RNA Immunoprecipitation for Determining RNA-Protein Associations In Vivo. *Curr Protoc Mol Biol* **75**, (2006).
19. Van Nostrand, E. L. *et al.* Robust transcriptome-wide discovery of RNA-binding protein binding sites with enhanced CLIP (eCLIP). *Nat Methods* **13**, 508–514 (2016).
20. Hafner, M. *et al.* Transcriptome-wide Identification of RNA-Binding Protein and MicroRNA Target Sites by PAR-CLIP. *Cell* **141**, 129–141 (2010).
21. Licatalosi, D. D. *et al.* HITS-CLIP yields genome-wide insights into brain alternative RNA processing. *Nature* **456**, 464–469 (2008).
22. Wang, S. *et al.* Enhancement of LIN28B-induced hematopoietic reprogramming by IGF2BP3. *Genes Dev.* **33**, 1048–1068 (2019).
23. Ule, J. *et al.* CLIP Identifies Nova-Regulated RNA Networks in the Brain. *Science* **302**, 1212–1215 (2003).
24. Horlacher, M. *et al.* A systematic benchmark of machine learning methods for protein–RNA interaction prediction. *Briefings in Bioinform* **24**, bbad307 (2023).
25. Orenstein, Y., Wang, Y. & Berger, B. RCK: accurate and efficient inference of sequence- and structure-based protein–RNA binding models from RNAcompete data. *Bioinformatics* **32**, i351–i359 (2016).
26. Maticzka, D., Lange, S. J., Costa, F. & Backofen, R. GraphProt: modeling binding preferences of RNA-binding proteins. *Genome Biol* **15**, R17 (2014).
27. Ben-Bassat, I., Chor, B. & Orenstein, Y. A deep neural network approach for learning intrinsic protein-RNA binding preferences. *Bioinformatics* **34**, i638–i646 (2018).
28. Alipanahi, B., Delong, A., Weirauch, M. T. & Frey, B. J. Predicting the sequence specificities of DNA- and RNA-binding proteins by deep learning. *Nat Biotechnol* **33**, 831–838 (2015).

29. Pan, X., Rijnbeek, P., Yan, J. & Shen, H.-B. Prediction of RNA-protein sequence and structure binding preferences using deep convolutional and recurrent neural networks. *BMC Genomics* **19**, 511 (2018).
30. Sun, L. *et al.* Predicting dynamic cellular protein–RNA interactions by deep learning using in vivo RNA structures. *Cell Res* **31**, 495–516 (2021).
31. Zhu, H. *et al.* Dynamic characterization and interpretation for protein-RNA interactions across diverse cellular conditions using HDRNet. *Nat Commun* **14**, 6824 (2023).
32. Zhao, W. *et al.* POSTAR3: an updated platform for exploring post-transcriptional regulation coordinated by RNA-binding proteins. *Nucleic Acids Res* **50**, D287–D294 (2022).
33. Zhang, Q., Wang, S., Li, Z., Pan, Y. & Huang, D.-S. Cross-Species Prediction of Transcription Factor Binding by Adversarial Training of a Novel Nucleotide-Level Deep Neural Network. *Adv Sci (Weinh)* **11**, e2405685 (2024).
34. Cochran, K. *et al.* Domain-adaptive neural networks improve cross-species prediction of transcription factor binding. *Genome Res.* **32**, 512–523 (2022).
35. Wang, J. *et al.* Generalizing to Unseen Domains: A Survey on Domain Generalization. *arXiv* https://doi.org/10.48550/ARXIV.2103.03097 (2021).
36. Lukasik, M., Bhojanapalli, S., Menon, A. K. & Kumar, S. Does label smoothing mitigate label noise? *arXiv* https://doi.org/10.48550/ARXIV.2003.02819 (2020).
37. Wang, Y. *et al.* Label smoothing regularization-based no hyperparameter domain generalization. *Knowledge-Based Systems* **309**, 112877 (2025).
38. Gerstberger, S., Hafner, M., Ascano, M. & Tuschl, T. Evolutionary conservation and expression of human RNA-binding proteins and their role in human genetic disease. *Adv Exp Med Biol* **825**, 1–55 (2014).
39. Beckmann, B. M. *et al.* The RNA-binding proteomes from yeast to man harbour conserved enigmRBPs. *Nat Commun* **6**, 10127 (2015).
40. Matia-González, A. M., Laing, E. E. & Gerber, A. P. Conserved mRNA-binding proteomes in eukaryotic organisms. *Nat Struct Mol Biol* **22**, 1027–1033 (2015).
41. Dominguez, D. *et al.* Sequence, Structure, and Context Preferences of Human RNA Binding Proteins. *Mol Cell* **70**, 854-867.e9 (2018).
42. Ray, D. *et al.* A compendium of RNA-binding motifs for decoding gene regulation. *Nature* **499**, 172–177 (2013).

43. Ramakrishnan, A. & Janga, S. C. Human protein-RNA interaction network is highly stable across mammals. *BMC Genomics* **20**, 1004 (2019).

44. Grishin, N. V. KH domain: one motif, two folds. *Nucleic Acids Research* **29**, 638–643 (2001).

45. Korn, S. M., Ulshöfer, C. J., Schneider, T. & Schlundt, A. Structures and target RNA preferences of the RNA-binding protein family of IGF2BPs: An overview. *Structure* **29**, 787–803 (2021).

46. Liu, Z.-P., Liu, S., Chen, R., Huang, X. & Wu, L.-Y. Structure alignment-based classification of RNA-binding pockets reveals regional RNA recognition motifs on protein surfaces. *BMC Bioinformatics* **18**, 27 (2017).

47. Irimia, M. *et al.* A Highly Conserved Program of Neuronal Microexons Is Misregulated in Autistic Brains. *Cell* **159**, 1511–1523 (2014).

48. Giudice, G., Sánchez-Cabo, F., Torroja, C. & Lara-Pezzi, E. ATtRACT-a database of RNA-binding proteins and associated motifs. *Database (Oxford)* **2016**, baw035 (2016).

49. Abramson, J. *et al.* Accurate structure prediction of biomolecular interactions with AlphaFold 3. *Nature* **630**, 493–500 (2024).

50. Budach, S. & Marsico, A. pysster: classification of biological sequences by learning sequence and structure motifs with convolutional neural networks. *Bioinformatics* **34**, 3035–3037 (2018).

51. UniProt Consortium. UniProt: the Universal Protein Knowledgebase in 2025. *Nucleic Acids Res* **53**, D609–D617 (2025).

52. Harris, S. E. *et al.* Understanding species-specific and conserved RNA-protein interactions in vivo and in vitro. *Nat Commun* **15**, (2024).

53. Bahrami-Samani, E. & Xing, Y. Discovery of Allele-Specific Protein-RNA Interactions in Human Transcriptomes. *Am J Hum Genet* **104**, 492–502 (2019).

54. Wu, K. *et al.* Exploring noncoding variants in genetic diseases: from detection to functional insights. *J Genet Genomics* **51**, 111–132 (2024).

55. Beaumont, C. *et al.* Mutation in the iron responsive element of the L ferritin mRNA in a family with dominant hyperferritinaemia and cataract. *Nat Genet* **11**, 444–446 (1995).

56. Van Nostrand, E. L. *et al.* A large-scale binding and functional map of human RNA-binding proteins. *Nature* **583**, 711–719 (2020).

57. Hu, L.-F. *et al.* Longitudinal and large-scale monitoring of transcriptome and RBP-RNA interactome in living cells by engineered protein nanocages. *bioRxiv* https://doi.org/10.1101/2025.03.13.642977 (2025).
58. Lau, A. W., Fukushima, H. & Wei, W. The Fbw7 and betaTRCP E3 ubiquitin ligases and their roles in tumorigenesis. *Front Biosci (Landmark Ed)* **17**, 2197–2212 (2012).
59. Herbst, A. *et al.* Methylation of helicase-like transcription factor in serum of patients with colorectal cancer is an independent predictor of disease recurrence. *Eur J Gastroenterol Hepatol* **21**, 565–569 (2009).
60. Gu, C. *et al.* TRIM50 inhibits glycolysis and the malignant progression of gastric cancer by ubiquitinating PGK1. *Int J Biol Sci* **20**, 3656–3674 (2024).
61. Zhao, C. *et al.* Repurposing an antidandruff agent to treating cancer: zinc pyrithione inhibits tumor growth via targeting proteasome-associated deubiquitinases. *Oncotarget* **8**, 13942–13956 (2017).
62. Xie, J. & Guo, Q. AATF protects neural cells against oxidative damage induced by amyloid beta-peptide. *Neurobiol Dis* **16**, 150–157 (2004).
63. Lee, S. *et al.* PTK2/FAK regulates UPS impairment via SQSTM1/p62 phosphorylation in TARDBP/TDP-43 proteinopathies. *Autophagy* **16**, 1396–1412 (2020).
64. Louros, S. R. & Osterweil, E. K. Perturbed proteostasis in autism spectrum disorders. *J Neurochem* **139**, 1081–1092 (2016).
65. Chua, J. P., De Calbiac, H., Kabashi, E. & Barmada, S. J. Autophagy and ALS: mechanistic insights and therapeutic implications. *Autophagy* **18**, 254–282 (2022).
66. Tollervey, J. R. *et al.* Characterizing the RNA targets and position-dependent splicing regulation by TDP-43. *Nat Neurosci* **14**, 452–458 (2011).
67. Seddighi, S. *et al.* Mis-spliced transcripts generate de novo proteins in TDP-43-related ALS/FTD. *Sci Transl Med* **16**, eadg7162 (2024).
68. Kellett, E. A., Bademosi, A. T. & Walker, A. K. Molecular mechanisms and consequences of TDP-43 phosphorylation in neurodegeneration. *Mol Neurodegener* **20**, 53 (2025).
69. Tran, N.-N. & Lee, B.-H. Functional implication of ubiquitinating and deubiquitinating mechanisms in TDP-43 proteinopathies. *Front Cell Dev Biol* **10**, 931968 (2022).
70. Kabashi, E. *et al.* TARDBP mutations in individuals with sporadic and familial amyotrophic lateral sclerosis. *Nat Genet* **40**, 572–574 (2008).

71. Xie, J. & Fu, T. DeepProtein: Deep Learning Library and Benchmark for Protein Sequence Learning. *Bioinformatics* (2025) doi:10.1093/bioinformatics/btaf165.
72. Uversky, V. N. Protein intrinsic disorder and structure-function continuum. *Prog Mol Biol Transl Sci* **166**, 1–17 (2019).
73. Nori, D. & Jin, W. RNAFlow: RNA Structure &amp; Sequence Design via Inverse Folding-Based Flow Matching. *arXiv* https://doi.org/10.48550/ARXIV.2405.18768 (2024).
74. Yamada, K. & Hamada, M. Prediction of RNA-protein interactions using a nucleotide language model. *Bioinform Adv* **2**, vbac023 (2022).
75. Liu, H., Jian, Y., Zeng, C. & Zhao, Y. RNA-protein interaction prediction using network-guided deep learning. *Commun Biol* **8**, 247 (2025).
76. Lukavsky, P. J. *et al.* Molecular basis of UG-rich RNA recognition by the human splicing factor TDP-43. *Nat Struct Mol Biol* **20**, 1443–1449 (2013).
77. Park, J., Cho, J. & Song, E. J. Ubiquitin-proteasome system (UPS) as a target for anticancer treatment. *Arch Pharm Res* **43**, 1144–1161 (2020).
78. RNAcentral Consortium. RNAcentral 2021: secondary structure integration, improved sequence search and new member databases. *Nucleic Acids Res* **49**, D212–D220 (2021).
79. Tamura, K., Stecher, G. & Kumar, S. MEGA11: Molecular Evolutionary Genetics Analysis Version 11. *Mol Biol Evol* **38**, 3022–3027 (2021).
80. Jumper, J. *et al.* Highly accurate protein structure prediction with AlphaFold. *Nature* **596**, 583–589 (2021).
81. Larkin, M. A. *et al.* Clustal W and Clustal X version 2.0. *Bioinformatics* **23**, 2947–2948 (2007).
82. Zhang, C., Shine, M., Pyle, A. M. & Zhang, Y. US-align: universal structure alignments of proteins, nucleic acids, and macromolecular complexes. *Nat Methods* **19**, 1109–1115 (2022).
83. Blum, M. *et al.* InterPro: the protein sequence classification resource in 2025. *Nucleic Acids Res* **53**, D444–D456 (2025).
84. Berman, H. M. *et al.* The Protein Data Bank. *Nucleic Acids Res* **28**, 235–242 (2000).
85. Lorenz, R. *et al.* ViennaRNA Package 2.0. *Algorithms Mol Biol* **6**, 26 (2011).
86. Bailey, T. L., Johnson, J., Grant, C. E. & Noble, W. S. The MEME Suite. *Nucleic Acids Res* **43**, W39–W49 (2015).

87. Zhou, T. *et al.* itol.toolkit accelerates working with iTOL (Interactive Tree Of Life) by an automated generation of annotation files. *Bioinformatics* btad339 (2023).
88. Jain, C., Koren, S., Dilthey, A., Phillippy, A. M. & Aluru, S. A fast adaptive algorithm for computing whole-genome homology maps. *Bioinformatics* **34**, i748–i756 (2018).
89. Edgar, R. C. Muscle5: High-accuracy alignment ensembles enable unbiased assessments of sequence homology and phylogeny. *Nat Commun* **13**, 6968 (2022).
90. Robinson, J. T. *et al.* Integrative genomics viewer. *Nat Biotechnol* **29**, 24–26 (2011).
91. Danecek, P. *et al.* Twelve years of SAMtools and BCFtools. *GigaScience* **10**, giab008 (2021).
92. Quinlan, A. R. & Hall, I. M. BEDTools: a flexible suite of utilities for comparing genomic features. *Bioinformatics* **26**, 841–842 (2010).
93. Harrison, P. W. *et al.* Ensembl 2024. *Nucleic Acids Res* **52**, D891–D899 (2024).
94. Altschul, S. F., Gish, W., Miller, W., Myers, E. W. & Lipman, D. J. Basic local alignment search tool. *J Mol Biol* **215**, 403–410 (1990).
95. Sun, L. *et al.* RNA structure maps across mammalian cellular compartments. *Nat Struct Mol Biol* **26**, 322–330 (2019).
96. Szklarczyk, D. *et al.* The STRING database in 2023: protein-protein association networks and functional enrichment analyses for any sequenced genome of interest. *Nucleic Acids Res* **51**, D638–D646 (2023).

Figure Legends

Figure 1: Evolutionary conservation of RBPs and their target RNAs

(a) Bar plots showing the sequence and structural similarity of RBPs across 11 species, in terms of full-length sequence (SeqS in blue), full-length structure (StrS in red), RBD sequence (DseqS in blue) and RBD structure (DStrS in red). The phylogenetic tree is constructed based on the 18S rRNA sequences in the 11 species, and shows the relative relationships between human and non-human species.

(b) Examples of structural alignment of homologous RBPs, including AGO2 (the highly conserved), DDX51 (the considerable conserved), RBM10 (the intermediately conserved), and SERBP1 (the weakly conserved). The RBP structure in human (red) is compared to that in non-human species (blue).

(c) SRRM4 binding distribution along meta-transcript in human (red line) and mouse (cyan line).

(d) Binding motif alignment of homologous RBPs in human (left) and mouse (right).

(e) Three-dimensional structure of RC3H1 in human (PDB ID 4QIL, left) and mouse (PDB ID 4QI2, right), showing bound RNA residues (orange), RBDs residues (blue), and other remaining RNA and protein residues (grey).

See also Supplementary Fig. 1 and 2.

Figure 2: The workflow of MuSIC

(a) Schematic showing the workflow of MuSIC. Step 1 (data pre-processing): collecting peaks of RBPs from multiple species, defining the positive and negative peaks, and constructing the training and validation set. Step 2 (feature engineering): encoding for the RBP-binding peaks and predicted RNA structures. Step 3 (Deep learning model): predicting RBP–RNA interactions using a CNN framework integrated with label smoothing strategy. Step 4 (Applications): comparing prediction performance with state-of-the-art computational methods, identifying and clustering RBP-binding motifs, analyzing conservation patterns of RBP-binding peaks, and quantifying the effects of SNVs on RBP binding.

(b) Flowchart showing data pre-processing and feature encoding. Top: positive (red) and negative (blue) peaks are encoded into one-hot vectors. Bottom: computationally predicted RNA structures are encoded into one-hot vectors.

(c) Diagram showing label smoothing strategy. Top left: using the image similarities between Cartoon and Sketch in computer vision for label smoothing strategy. Top right: using the RBP similarities between human (blue) and mouse (red) for label smoothing. Bottom: transforming the one-hot labels into smoothed labels based on RBP conservation and computing cross-entropy loss for both one-hot labels and smoothed labels.

(d) Diagram showing two components of the total loss L_{total}, L_{ture} (human in black) and L_{smooth} (mouse in red).

(e) Overview of the deep learning model architecture. One-hot encoded input (b) is processed sequentially through the convolutional layers, SE modules, residual blocks, max pooling, and fully connected layers to predict the binding probability.

(f) Boxplot showing the prediction performance for different types of input features, including only sequence (101nt / 200nt) (blue), 200nt sequence with label smoothing (green), sequence with label smoothing and predicted structure (red).

See also **Supplementary Fig. 3**.

Figure 3: Comparison of prediction performance between MuSIC and other computational methods

(a) Violin plot showing the prediction accuracy of MuSIC (red) and other computational methods (blue) for 19 cross-species datasets. *** $P < 0.005$, paired paired t-test.

(b) ROC curves showing the prediction accuracy of MuSIC (red) and other computational methods (blue) for two RBPs, YTHDC2 (left) and TAF15 (right).

(c) t-SNE clustering showing the output feature maps by MuSIC and other computational methods for separating the positive (cyan) and negative (grey) peaks.

(d) Bar plot showing the overlapping ratio between the experimentally-derived and predicted peaks by MuSIC (red) and other computational methods (blue). *** $P < 0.005$, paired t-test; ****, $P < 0.0001$, paired t-test.

(e) Heatmap showing the overlapping ratio between the experimentally-derived and predicted peaks by MuSIC and other computational methods.

(f) An example of predicted peaks distribution along the local region in mouse genome (chr7:96,200,000–96,400,000). Red indicates true positives and black indicates false negatives, as evaluated against the experimentally-derived peaks.

See also **Supplementary Fig. 4, 5** and **6**.

Figure 4: Reliable predictions of RBP-binding peaks and motif clustering by MuSIC

(a) Scatter plot showing the correlation between the cross-species prediction accuracy and RBP conservation for the 14 RBPs (mouse in red, zebrafish in blue).

(b) Examples showing the consistency of the predicted binding motifs and experimentally-derived motifs (from ATtRACT database) of several RBPs.

(c) Hierarchical clustering of 186 predicted binding motifs in human, mouse, zebrafish, and yeast. Stars indicate that there are no motifs enriched.

See also **Supplementary Fig. 7** and **8**.

Figure 5: Cross-species conservation of RBP-binding peaks

(a) Heatmap showing the percentage of homologous transcripts containing the conserved peaks bound by RBPs across the 11 species, where all the 186 RBPs can be categorized into three groups. Boxplot showing the conservation degree (measured by percentage of species) of the homologous transcripts containing the conserved peaks.

(b) Examples showing the predicted peaks bound by RBM15B and ALKBH1 along the transcript ENST00000688663.1.

(c) Forest plot showing the conservation of the peaks bound by the CPSF family. We include the predicted peaks ranging from human to each of the non-human species shown here according to the phylogenetic tree.

See also Supplementary Fig. 9.

Figure 6: RBP–RNA interactions affected by SNVs and their associations with human diseases

(a) The experimentally-derived and predicted effects of SNVs on SRSF1 and DDX3X binding. Obs.REF, the binding strength from CLIP-seq data for the reference allele; Obs.ALT, the binding strength from CLIP-seq data for the alternative allele; Pre.REF, the binding strength from MuSIC prediction for the reference allele; and Pre.ALT, the binding strength from MuSIC prediction for the alternative allele.

(b) Consistency between the experimentally-derived and predicted effects of SNVs on RBP binding for the 186 RBPs. Green bar indicates high consistency ($-\log FDR \geqslant 1.3$), whereas grey bar indicates no significance.

(c) Schematic showing the workflow for quantifying the effects of homologous SNVs on RBP binding.

(d) An example showing the effect of a homologous SNV (NC_000006.11: g.4059022A>G) on PUM2 binding in human. The saliency maps show the predicted effect of REF (A) (top) and ALT (G) (bottom) on PUM2 binding. In each saliency map, the two heatmap tracks display the sequence response (top) and structure response (bottom) of the model at the base level. The homologous SNV position is highlighted by a dashed box.

(e) An example showing the effect of a homologous SNV (ENSMUST00000220965.2 1446 A>G) on PUM2 binding in mouse. The saliency maps show the predicted effect of REF (A) (top) and ALT (G) (bottom) on PUM2 binding.

(f) Examples showing *in vitro* RNA pull-down assays (n = 3) examining the effects of three homologous SNVs on PUM2 binding in human (top) and mouse (bottom).

(g) Examples showing *in vivo* POND-qPCR (n = 3) quantification of REF/ALT target RNAs binding to human and mouse PUM2 in HEK293T. Relative RNA enrichment was calculated as: (RNA ^{supernatant}/ERCC spike-in)/ (RNA ^{cellular}/GAPDH). Then the

ALT group was normalized to the REF group. Green bar represents RNA enrichment for REF sequences, and blue bar for ALT sequences.

(h) Enriched biological functions of the SNV-affected transcripts. The 186 RBPs can be categorized into four groups according to the enriched functions of their target transcripts. In total, 21 RBPs are identified as highly ubiquitin-related, some of which have been revealed as associated with neurodegenerative diseases (red) and cancer (blue).

See also **Supplementary Fig. 10, 11, 12** and **13**.

Supplementary Figure Legends

Supplementary Figure 1: Evolutionary conservation of RBPs across 11 species

(a-b) Heatmaps showing the full-length sequence similarity (a) and structural similarity (b) of RBPs across species.

(c-d) Heatmaps showing the RBD sequence similarity (c) and structural similarity (d) of RBPs across species

Supplementary Figure 2: Evolutionary conservation of RBP-targeted RNAs

(a) LIN28A binding distribution along meta-transcript in human (red line) and mouse (cyan line).

(b-c) Three-dimensional structures of IGF2BP1 in human (b) and mouse (c), showing the bound RNA residues and three KH domains residues.

(d-e) Heatmaps showing residue interaction score for IGF2BP1 in human (d) and mouse (e), with darker green represents stronger interaction scores.

(f) Venn diagrams showing the overlap of RBPs between different species (human, mouse, zebrafish, fly, worm, *A. thaliana*, and yeast) collected from POSTAR3 database.

Supplementary Figure 3: Optimization of input feature and model architecture

(a) Boxplot showing the prediction performance for different input sequence length (101nt, 200nt, and 400nt) on MuSIC performance. *** $P < 0.005$, paired t-test.

(b) Boxplot showing the prediction performance of label smoothing, including only sequence (blue), and sequence with label smoothing (green). ** $P < 0.01$, paired t-test.

(c) Boxplot showing the prediction performance of different structural features, including only predicted structure (cyan), only sequence (blue), sequence with predicted structure (red), and sequence with experimentally-measured structure (red).

(d) t-SNE clustering showing the output feature maps by different blocks (input, SE block, residual block, FCL) for separating the positive (cyan) and negative (grey) peaks.

(e) Boxplot showing the prediction accuracy of MuSIC (red) and other machine learning models (grey). **** $P < 0.001$, paired t-test.

(f) Boxplot showing the prediction accuracy of MuSIC (red) and other deep learning models (grey). * $P < 0.05$, ** $P < 0.01$, **** $P < 0.001$, paired t-test.

Supplementary Figure 4: The performance comparison between MuSIC and other computational methods

(a) Violin plot showing the prediction accuracy of MuSIC (red) and other computational methods (blue) across 224 within-species datasets. * $P < 0.05$, *** $P < 0.005$, paired t-test.

(b-c) Violin plot showing the prediction accuracy (PRAUC and ACC) of MuSIC (red) and other computational methods (blue) across 19 cross-species datasets. *** $P < 0.005$, paired t-test.

(d) Violin plot showing the prediction accuracy of MuSIC (red) and other computational methods (blue) across 38 cross-species datasets. ** $P < 0.01$, *** $P < 0.005$, paired t-test.

(e) Violin plot showing the prediction accuracy of MuSIC (red) and other computational methods (blue) across 17 cross-species datasets. *** $P < 0.005$, paired t-test.

(f) Violin plot showing the prediction accuracy of MuSIC (red) and other computational methods (gradient blue) across 8 cross-species datasets. * $P < 0.05$, *** $P < 0.005$, paired t-test.

Supplementary Figure 5: Comparison of feature learning discriminative power between MuSIC and other computational methods

(a) ROC curves showing the prediction accuracy of MuSIC (red) and other computational methods (blue) for 6 RBPs, 2RBPs for human (left), 2 RBPs for mouse (middle), and 2 RBPs for zebrafish (right).

(b) t-SNE clustering showing the output feature maps by MuSIC and other computational methods for separating the positive (cyan) and negative (grey) peaks.

Supplementary Figure 6: Consistency of RBP-binding distributions between MuSIC predictions and experimental data

(a-b) ELAVL1 binding distributions along meta-transcript in MuSIC predictions (red line) and experimentally-derived data (black line). Scatter plot showing the correlation of RBP-binding distributions from MuSIC predictions and experimental data for ELAVL1.

(c) Scatter plot showing the correlation of RBP-binding distributions from MuSIC predictions and experimental data for 23 RBPs.

Supplementary Figure 7: Evolutionary conservation of high-confidence RBP-binding motifs

(a) Flowchart showing the calculation of RBP conservation.

(b) Scatter plot showing the correlation between the MuSIC-predicted accuracy and RBP conservation for RBPs from the 10 non-human species.

(c) Examples showing the consistency of the predicted binding motifs and experimentally-derived motifs (from ATtRACT database) of several RBPs.

(d) Examples showing high-confidence RBP-binding motifs across the 11 species, including human, orangutan, monkey, mouse, rat, chicken, frog, zebrafish, fly, *A. thaliana*, and yeast.

Supplementary Figure 8: Clustering of RBP-binding motifs

Hierarchical clustering of 186 predicted binding motifs in human, orangutan, monkey, rat, chicken, frog, fly, and yeast. Stars indicate that there are no motifs enriched.

Supplementary Figure 9: Cross-species conservation of predicted RBP-binding peaks

(a) Schematic showing the workflow for cross-species RBP-binding peaks conservation analysis.

(b) Histogram showing the conservation of RBP-binding peaks across 11 species for 186 RBPs.

(c) Boxplot showing the conservation degree of RBP-binding peaks across 11 species for CPSF family (top) and YTH (bottom) family.

(d) Forest plot showing the conservation of the peaks bound by the YTH family. We include the predicted peaks ranging from human to each of the non-human species shown here according to the phylogenetic tree.

Supplementary Figure 10: Consistency between the predicted and experimentally-derived effects of SNVs on RBP–RNA interactions

(a) Schematic showing the workflow for separating peak signals into the REF and ALT groups. *** $P < 0.005$, unpaired t-test.

(b) Schematic showing the workflow for evaluating consistency of SNV effects between MuSIC predictions and experimental data.

Supplementary Figure 11: Experimental validations for the predicted effects of SNVs on RBP–RNA interactions in human and mouse

(a) Flowchart of using the POND method to detect the interaction between PUM2 and REF/ALT target RNA. PUM2 is fused to the C-terminus of the EPN24 nanocage monomer, while REF and ALT RNA targets are cloned into the 3'UTR of GFP on a separate plasmid. In HEK293T cells, EPN24-PUM2 is co-transfected with either GFP-REF or GFP-ALT RNA target plasmids. After transfection, EPN24-PUM2 packaged target RNAs into extracellular supernatant. Both supernatant and cells are collected for RNA extraction, followed by analysis of differential enrichment between REF and ALT target RNAs with RT-qPCR.

(b) RNA pull-down assays and immunoblots for human PUM2 (left) and mouse PUM2 (right). Biotin-labeled REF and ALT RNA probes were used to perform RNA pull-down assays from lysates of 293T cells overexpressing myc-tagged PUM2. The pulled-down complexes were then analyzed by immunoblotting to detect the presence of PUM2 protein. The upper blot represents the results of repeat 2, and the lower blot represents the results of repeat 3.

(c) Bar plot quantifying *in vitro* RNA pull-down (n = 3) enrichment of human and mouse PUM2 protein binding to REF and ALT target RNAs. For each condition, pulled-down PUM2 levels were normalized to PUM2 in the input lysate. Then the ALT group was normalized to the REF group. Green bars represent REF sequences, and blue bars represent ALT sequences. All *P* values are calculated using two-tailed unpaired Student's t-test.

Supplementary Figure 12: Predicted effects of SNVs on RBP–RNA interactions and their associations with human diseases

(a) Schematic showing the workflow of biological function enrichment analysis for RBPs affected by SNVs.

(b) Bar chart showing the terms of biological functions associated with the weakly ubiquitin-related RBPs.

(c) Sankey diagram showing the potential regulatory associations among SNVs, RBPs, and UPS-related disease.

Supplementary Figure 13: Predicted effects of SNVs on TARDBP binding and the enriched biological functions of the transcripts containing the SNVs

(a) An example showing the effect of a homologous SNV (ENSMUST00000239066 1473 U>C) on TARDBP binding in mouse. The saliency maps show the predicted effect of REF (U) (top) and ALT (C) (bottom) on TARDBP binding.

(b) Gene Ontology enrichment result showing the biological process pathways for the TARDBP-bound genes perturbed by SNVs.

(c) Reactome pathway enrichment result showing the biological functions for TARDBP-bound genes perturbed by SNVs.

Supplementary Table Legends

Supplementary Table 1: Evolutionary conservation of RBPs across 11 species

Supplementary Table 2: Conservation-based grouping of 216 RBPs

Supplementary Table 3: MuSIC training and validation datasets

Supplementary Table 4: Prediction performance of MuSIC

Supplementary Table 5: Predicted RBP-binding motifs from MuSIC

Supplementary Table 6: Consistency of SNV effects

Supplementary Table 7: Experimental validation of SNV effects

Supplementary Table 8: Functional enrichment of SNV-affected genes

Figure 1

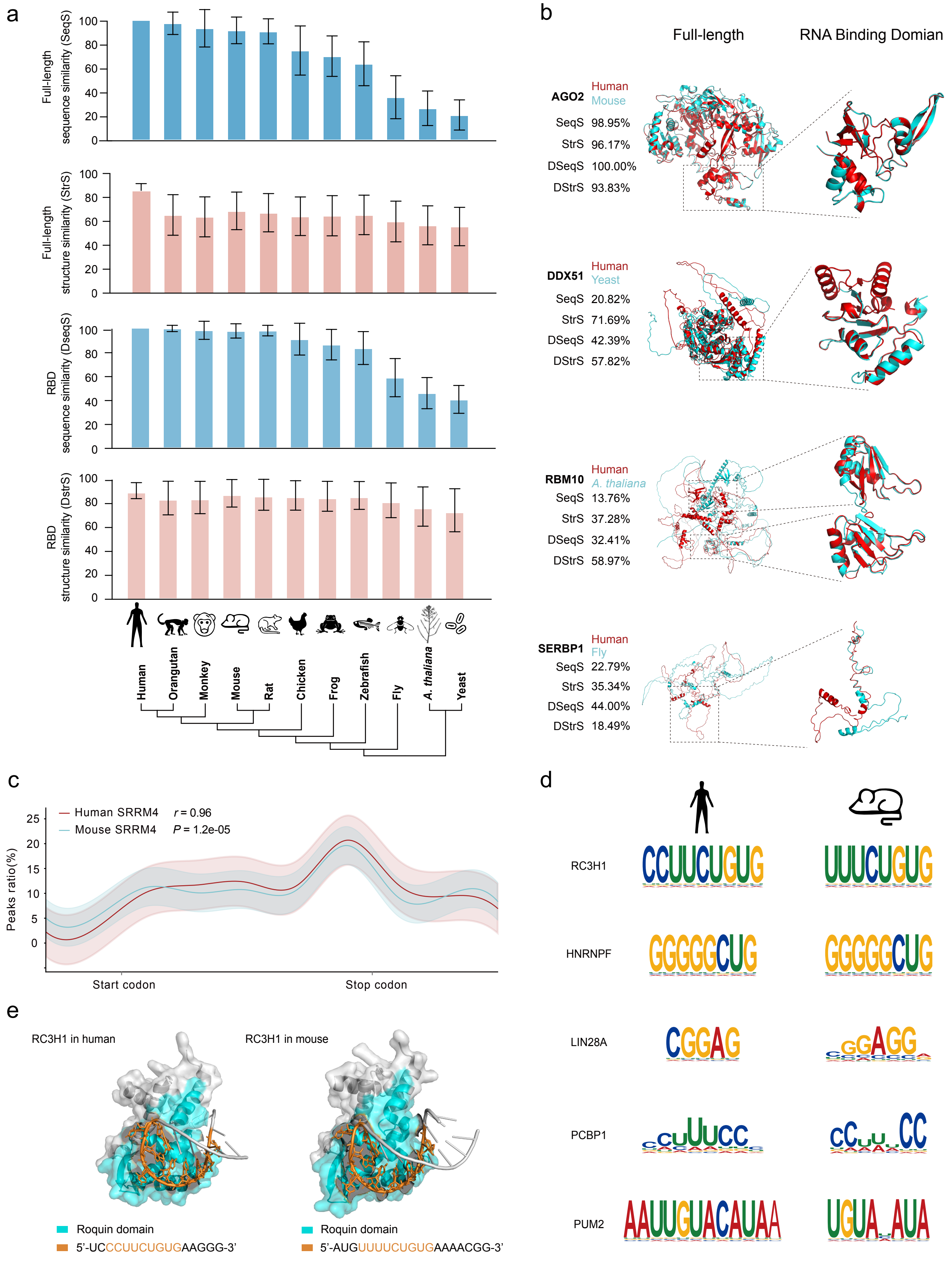
a
Full-length sequence similarity (SeqS)
Full-length structure similarity (StrS)
RBD sequence similarity (DseqS)
RBD structure similarity (DstrS)
0
20
40
60
80
100
Human
Orangutan
Monkey
Mouse
Rat
Chicken
Frog
Zebrafish
Fly
A. thaliana
Yeast
b
Full-length
RNA Binding Domian
AGO2
Human
Mouse
SeqS 98.95%
StrS 96.17%
DSeqS 100.00%
DStrS 93.83%
DDX51
Human
Yeast
SeqS 20.82%
StrS 71.69%
DSeqS 42.39%
DStrS 57.82%
RBM10
Human
A. thaliana
SeqS 13.76%
StrS 37.28%
DSeqS 32.41%
DStrS 58.97%
SERBP1
Human
Fly
SeqS 22.79%
StrS 35.34%
DSeqS 44.00%
DStrS 18.49%
c
Human SRRM4
Mouse SRRM4
r = 0.96
P = 1.2e-05
Peaks ratio(%)
0
5
10
15
20
25
Start codon
Stop codon
d
RC3H1
CCUUCUGUG
UUUCUGUG
HNRNPF
GGGGGCUG
GGGGGCUG
LIN28A
CGGAG
GGAGG
PCBP1
CCUUUCC
CCUUCC
PUM2
AAUUGUACAUAA
UGUA AUA
e
RC3H1 in human
RC3H1 in mouse
Roquin domain
5'-UCCCUUCUGUGAAGGG-3'
Roquin domain
5'-AUGUUUUCUGUGAAAACGG-3'

Figure 2

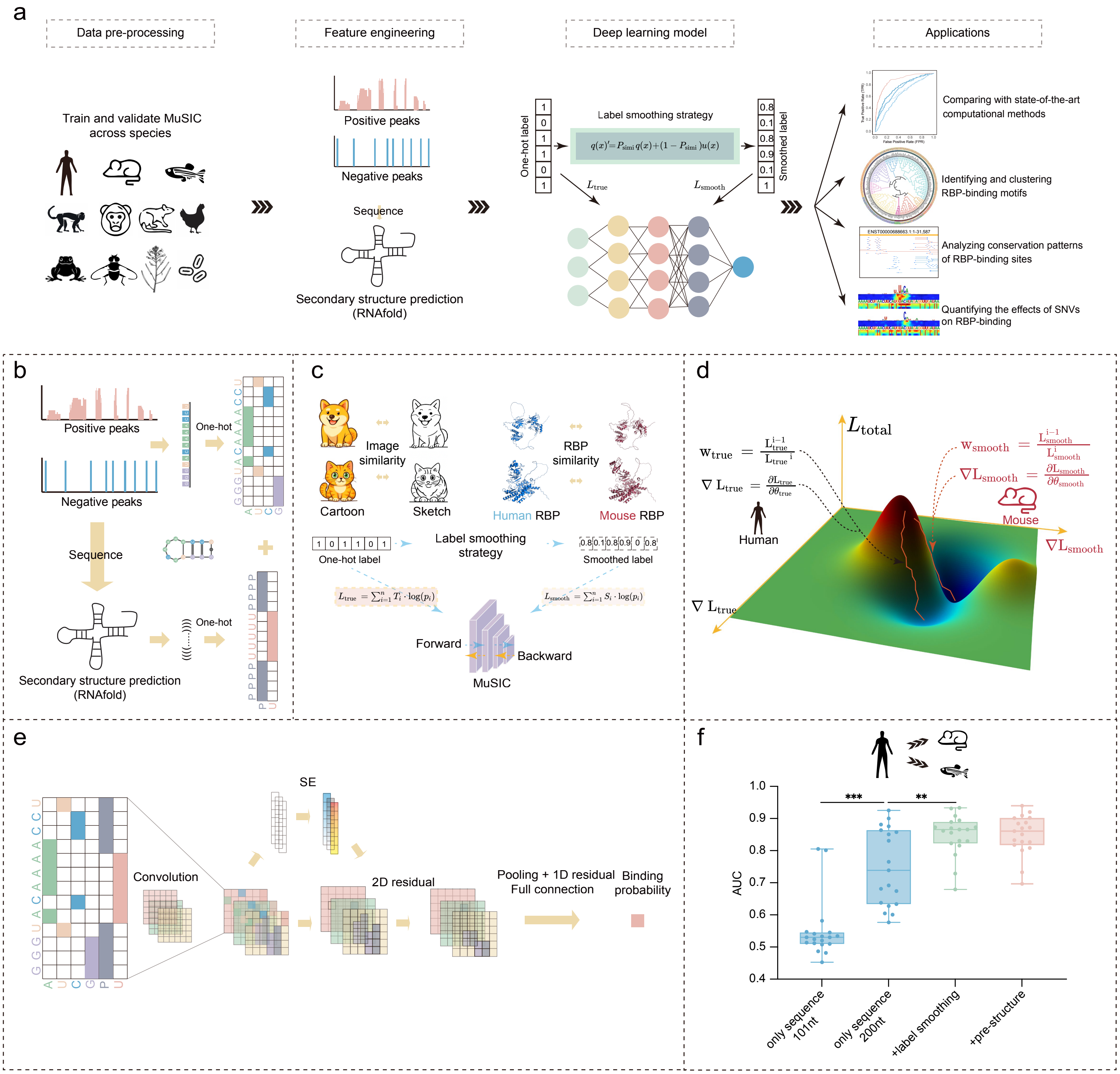
a
Data pre-processing
Feature engineering
Deep learning model
Applications
Train and validate MuSIC across species
Positive peaks
Negative peaks
Sequence
Secondary structure prediction (RNAfold)
Label smoothing strategy
$q(x)' = P_{\mathrm{simi}}\, q(x) + (1 - P_{\mathrm{simi}})\, u(x)$
One-hot label
1 0 1 1 0 1
Smoothed label
0.8 0.1 0.8 0.9 0.1 1
L_{true}
L_{smooth}
Comparing with state-of-the-art computational methods
Identifying and clustering RBP-binding motifs
Analyzing conservation patterns of RBP-binding sites
Quantifying the effects of SNVs on RBP-binding
b
Positive peaks
Negative peaks
One-hot
Sequence
Secondary structure prediction (RNAfold)
One-hot
c
Image similarity
Cartoon
Sketch
RBP similarity
Human RBP
Mouse RBP
One-hot label
1 0 1 1 0 1
Label smoothing strategy
Smoothed label
0.8 0.1 0.8 0.9 0 0.8
$L_{\mathrm{true}} = \sum_{i=1}^{n} T_i \cdot \log(p_i)$
$L_{\mathrm{smooth}} = \sum_{i=1}^{n} S_i \cdot \log(p_i)$
Forward
Backward
MuSIC
d
L_{total}
$w_{\mathrm{true}} = \frac{L_{\mathrm{true}}^{i-1}}{L_{\mathrm{true}}^{i}}$
$\nabla L_{\mathrm{true}} = \frac{\partial L_{\mathrm{true}}}{\partial \theta_{\mathrm{true}}}$
Human
$w_{\mathrm{smooth}} = \frac{L_{\mathrm{smooth}}^{i-1}}{L_{\mathrm{smooth}}^{i}}$
$\nabla L_{\mathrm{smooth}} = \frac{\partial L_{\mathrm{smooth}}}{\partial \theta_{\mathrm{smooth}}}$
Mouse
$\nabla L_{\mathrm{smooth}}$
∇L_{true}
e
Convolution
SE
2D residual
Pooling + 1D residual Full connection
Binding probability
f
1.0
0.9
0.8
0.7
0.6
0.5
0.4
AUC
***
**
only sequence 101nt
only sequence 200nt
+label smoothing
+pre-structure

Figure 3

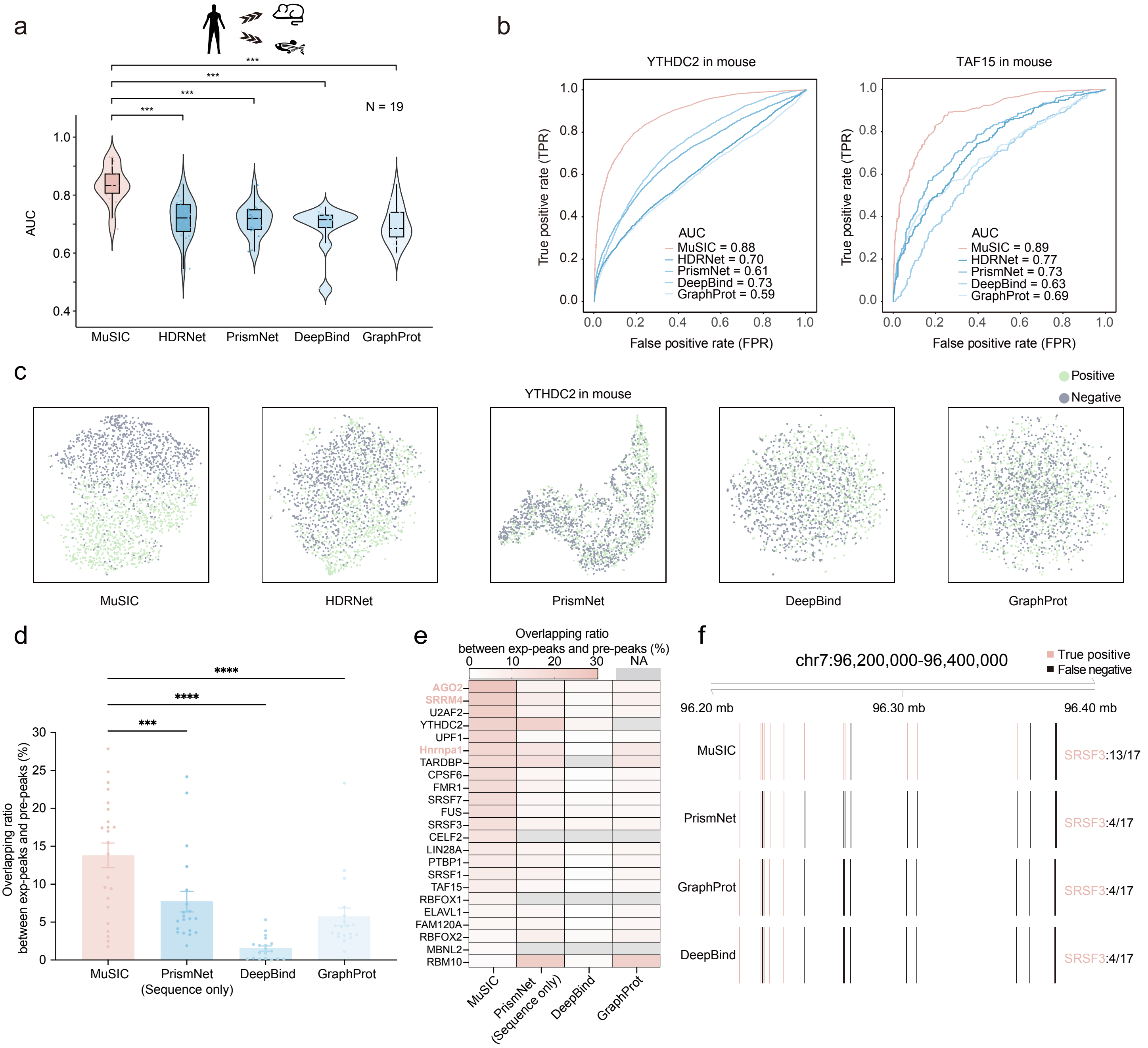
a
***
***
***
***
N = 19
AUC
1.0
0.8
0.6
0.4
MuSIC
HDRNet
PrismNet
DeepBind
GraphProt
b
YTHDC2 in mouse
TAF15 in mouse
True positive rate (TPR)
False positive rate (FPR)
0.0
0.2
0.4
0.6
0.8
1.0
AUC
MuSIC = 0.88
HDRNet = 0.70
PrismNet = 0.61
DeepBind = 0.73
GraphProt = 0.59
AUC
MuSIC = 0.89
HDRNet = 0.77
PrismNet = 0.73
DeepBind = 0.63
GraphProt = 0.69
c
YTHDC2 in mouse
Positive
Negative
MuSIC
HDRNet
PrismNet
DeepBind
GraphProt
d
****
****
***
Overlapping ratio
between exp-peaks and pre-peaks (%)
30
25
20
15
10
5
0
MuSIC
PrismNet
(Sequence only)
DeepBind
GraphProt
e
Overlapping ratio
between exp-peaks and pre-peaks (%)
0
10
20
30
NA
AGO2
SRRM4
U2AF2
YTHDC2
UPF1
Hnrnpa1
TARDBP
CPSF6
FMR1
SRSF7
FUS
SRSF3
CELF2
LIN28A
PTBP1
SRSF1
TAF15
RBFOX1
ELAVL1
FAM120A
RBFOX2
MBNL2
RBM10
MuSIC
PrismNet
(Sequence only)
DeepBind
GraphProt
f
chr7:96,200,000-96,400,000
True positive
False negative
96.20 mb
96.30 mb
96.40 mb
MuSIC
PrismNet
GraphProt
DeepBind
SRSF3:13/17
SRSF3:4/17
SRSF3:4/17
SRSF3:4/17

Figure 4

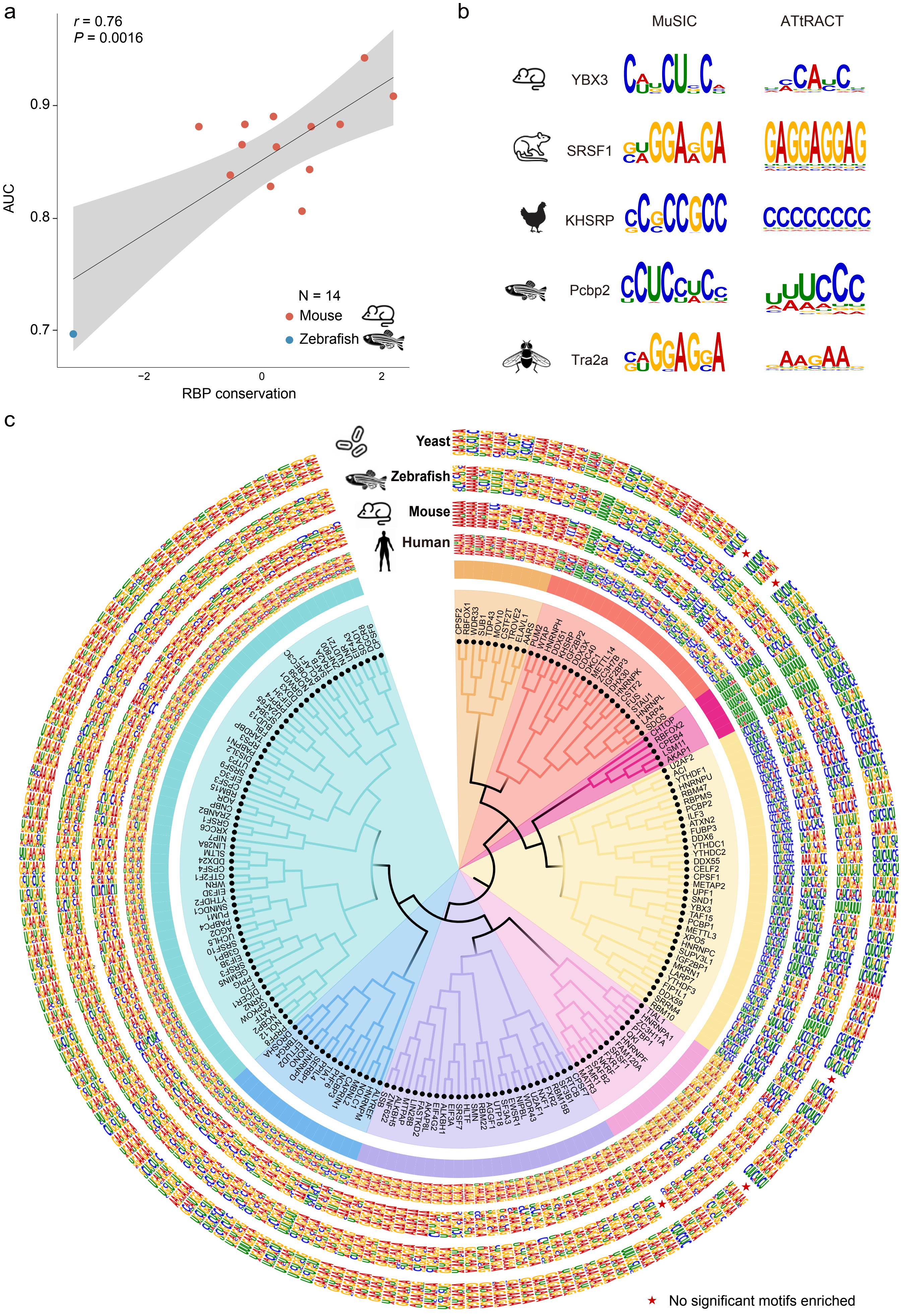
a
r = 0.76
P = 0.0016
AUC
0.9
0.8
0.7
−2
0
2
RBP conservation
N = 14
Mouse
Zebrafish
b
MuSIC
ATtRACT
YBX3
SRSF1
KHSRP
Pcbp2
Tra2a
c
Yeast
Zebrafish
Mouse
Human
★ No significant motifs enriched

Figure 5

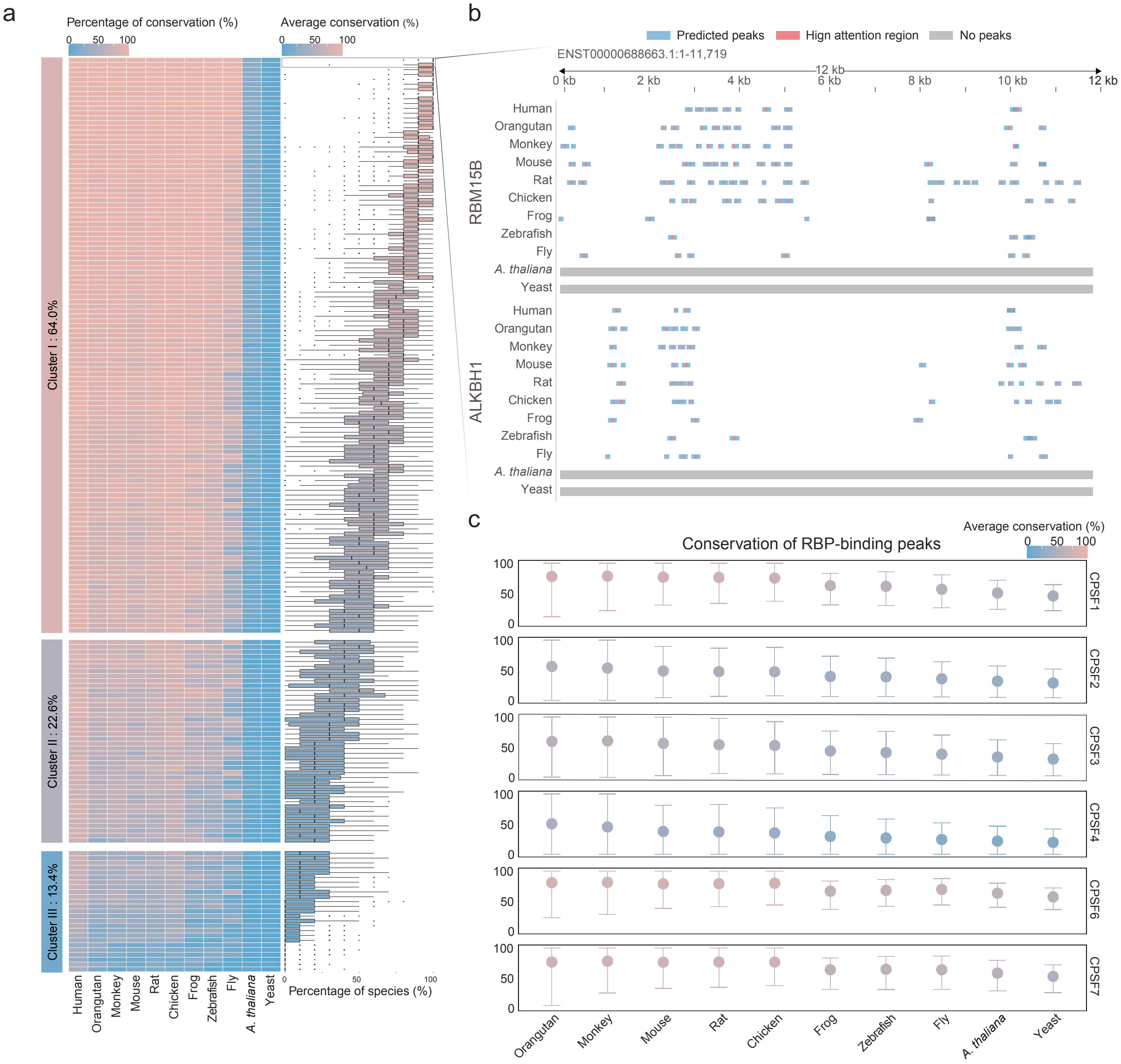
a
Percentage of conservation (%)
0 50 100
Average conservation (%)
0 50 100
Cluster I : 64.0%
Cluster II : 22.6%
Cluster III : 13.4%
Human
Orangutan
Monkey
Mouse
Rat
Chicken
Frog
Zebrafish
Fly
A. thaliana
Yeast
0 50 100
Percentage of species (%)
b
Predicted peaks
Hign attention region
No peaks
ENST00000688663.1:1-11,719
12 kb
0 kb
2 kb
4 kb
6 kb
8 kb
10 kb
12 kb
RBM15B
ALKBH1
Human
Orangutan
Monkey
Mouse
Rat
Chicken
Frog
Zebrafish
Fly
A. thaliana
Yeast
c
Conservation of RBP-binding peaks
Average conservation (%)
0 50 100
CPSF1
CPSF2
CPSF3
CPSF4
CPSF6
CPSF7
0
50
100
Orangutan
Monkey
Mouse
Rat
Chicken
Frog
Zebrafish
Fly
A. thaliana
Yeast

Figure 6

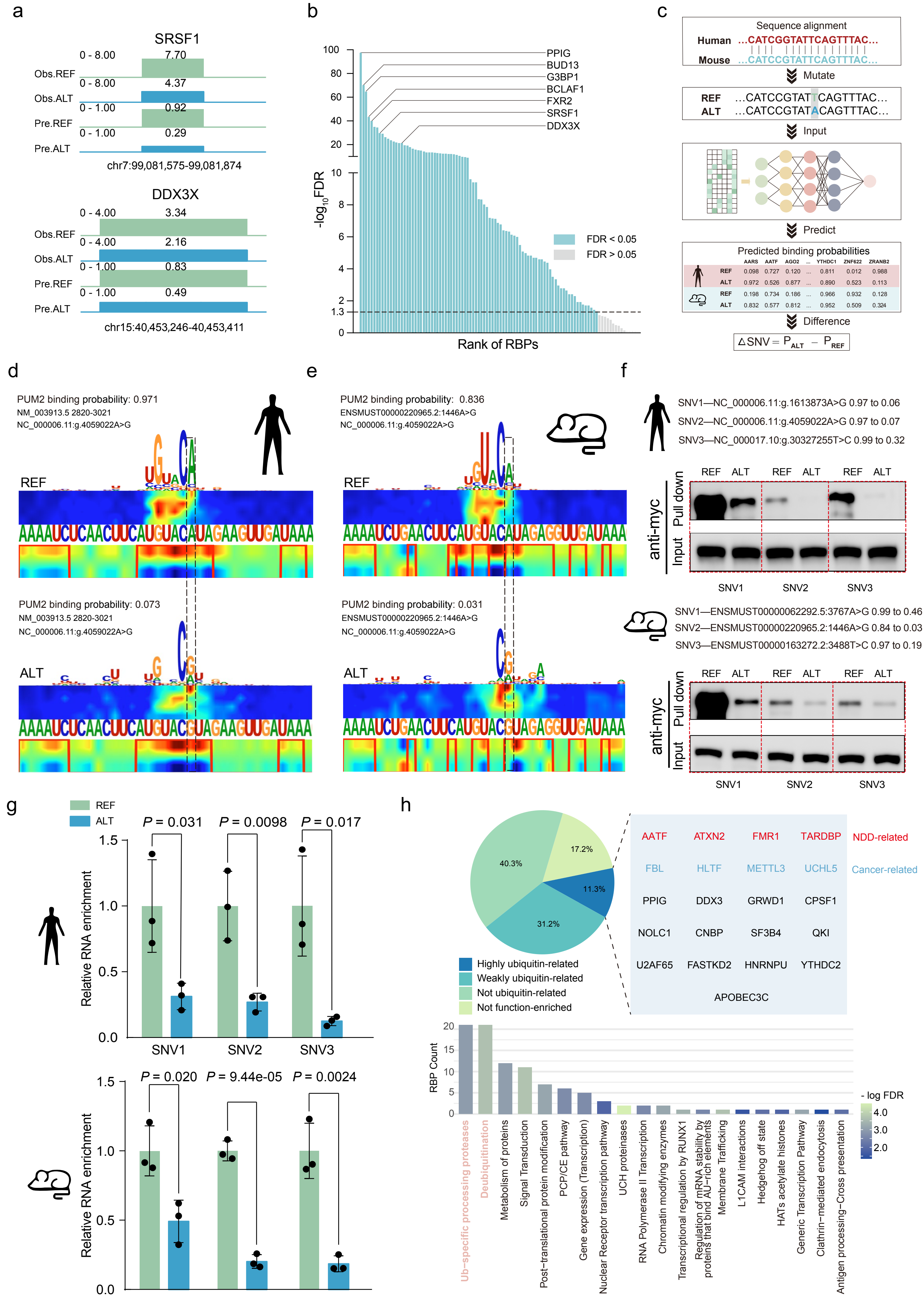
a
SRSF1
0 - 8.00
7.70
Obs.REF
0 - 8.00
4.37
Obs.ALT
0 - 1.00
0.92
Pre.REF
0 - 1.00
0.29
Pre.ALT
chr7:99,081,575-99,081,874
DDX3X
0 - 4.00
3.34
Obs.REF
0 - 4.00
2.16
Obs.ALT
0 - 1.00
0.83
Pre.REF
0 - 1.00
0.49
Pre.ALT
chr15:40,453,246-40,453,411
b
PPIG
BUD13
G3BP1
BCLAF1
FXR2
SRSF1
DDX3X
-log10FDR
100
80
60
40
20
10
8
6
4
2
1.3
0
FDR < 0.05
FDR > 0.05
Rank of RBPs
c
Sequence alignment
Human ...CATCGGTATTCAGTTTAC...
Mouse ...CATCCGTATTCAGTTTAC...
Mutate
REF ...CATCCGTATTCAGTTTAC...
ALT ...CATCCGTATACAGTTTAC...
Input
Predict
Predicted binding probabilities
AARS AATF AGO2 ... YTHDC1 ZNF622 ZRANB2
REF 0.098 0.727 0.120 ... 0.811 0.012 0.988
ALT 0.972 0.526 0.877 ... 0.890 0.523 0.113
REF 0.198 0.734 0.186 ... 0.966 0.932 0.128
ALT 0.832 0.577 0.812 ... 0.952 0.509 0.324
Difference
ΔSNV = P_ALT − P_REF
d
PUM2 binding probability: 0.971
NM_003913.5 2820-3021
NC_000006.11:g.4059022A>G
REF
AAAAUCUCAACUUCAUGUACAUAGAAGUUGAUAAA
PUM2 binding probability: 0.073
NM_003913.5 2820-3021
NC_000006.11:g.4059022A>G
ALT
AAAAUCUCAACUUCAUGUACGUAGAAGUUGAUAAA
e
PUM2 binding probability: 0.836
ENSMUST00000220965.2:1446A>G
NC_000006.11:g.4059022A>G
REF
AAAAUCUGAACUUCAUGUACAUAGAGGUUGAUAAA
PUM2 binding probability: 0.031
ENSMUST00000220965.2:1446A>G
NC_000006.11:g.4059022A>G
ALT
AAAAUCUGAACUUCAUGUACGUAGAGGUUGAUAAA
f
SNV1—NC_000006.11:g.1613873A>G 0.97 to 0.06
SNV2—NC_000006.11:g.4059022A>G 0.97 to 0.07
SNV3—NC_000017.10:g.30327255T>C 0.99 to 0.32
REF ALT REF ALT REF ALT
anti-myc
Pull down
Input
SNV1 SNV2 SNV3
SNV1—ENSMUST00000062292.5:3767A>G 0.99 to 0.46
SNV2—ENSMUST00000220965.2:1446A>G 0.84 to 0.03
SNV3—ENSMUST00000163272.2:3488T>C 0.97 to 0.19
REF ALT REF ALT REF ALT
anti-myc
Pull down
Input
SNV1 SNV2 SNV3
g
REF
ALT
P = 0.031
P = 0.0098
P = 0.017
1.5
1.0
0.5
0.0
Relative RNA enrichment
SNV1 SNV2 SNV3
P = 0.020
P = 9.44e-05
P = 0.0024
1.5
1.0
0.5
0.0
Relative RNA enrichment
SNV1 SNV2 SNV3
h
40.3%
17.2%
11.3%
31.2%
Highly ubiquitin-related
Weakly ubiquitin-related
Not ubiquitin-related
Not function-enriched
AATF ATXN2 FMR1 TARDBP NDD-related
FBL HLTF METTL3 UCHL5 Cancer-related
PPIG DDX3 GRWD1 CPSF1
NOLC1 CNBP SF3B4 QKI
U2AF65 FASTKD2 HNRNPU YTHDC2
APOBEC3C
RBP Count
20
15
10
5
0
Ub-specific processing proteases
Deubiquitination
Metabolism of proteins
Signal Transduction
Post-translational protein modification
PCP/CE pathway
Gene expression (Transcription)
Nuclear Receptor transcription pathway
UCH proteinases
RNA Polymerase II Transcription
Chromatin modifying enzymes
Transcriptional regulation by RUNX1
Regulation of mRNA stability by proteins that bind AU-rich elements
Membrane Trafficking
L1CAM interactions
Hedgehog off state
HATs acetylate histones
Generic Transcription Pathway
Clathrin-mediated endocytosis
Antigen processing-Cross presentation
- log FDR
4.0
3.0
2.0

Figure S1

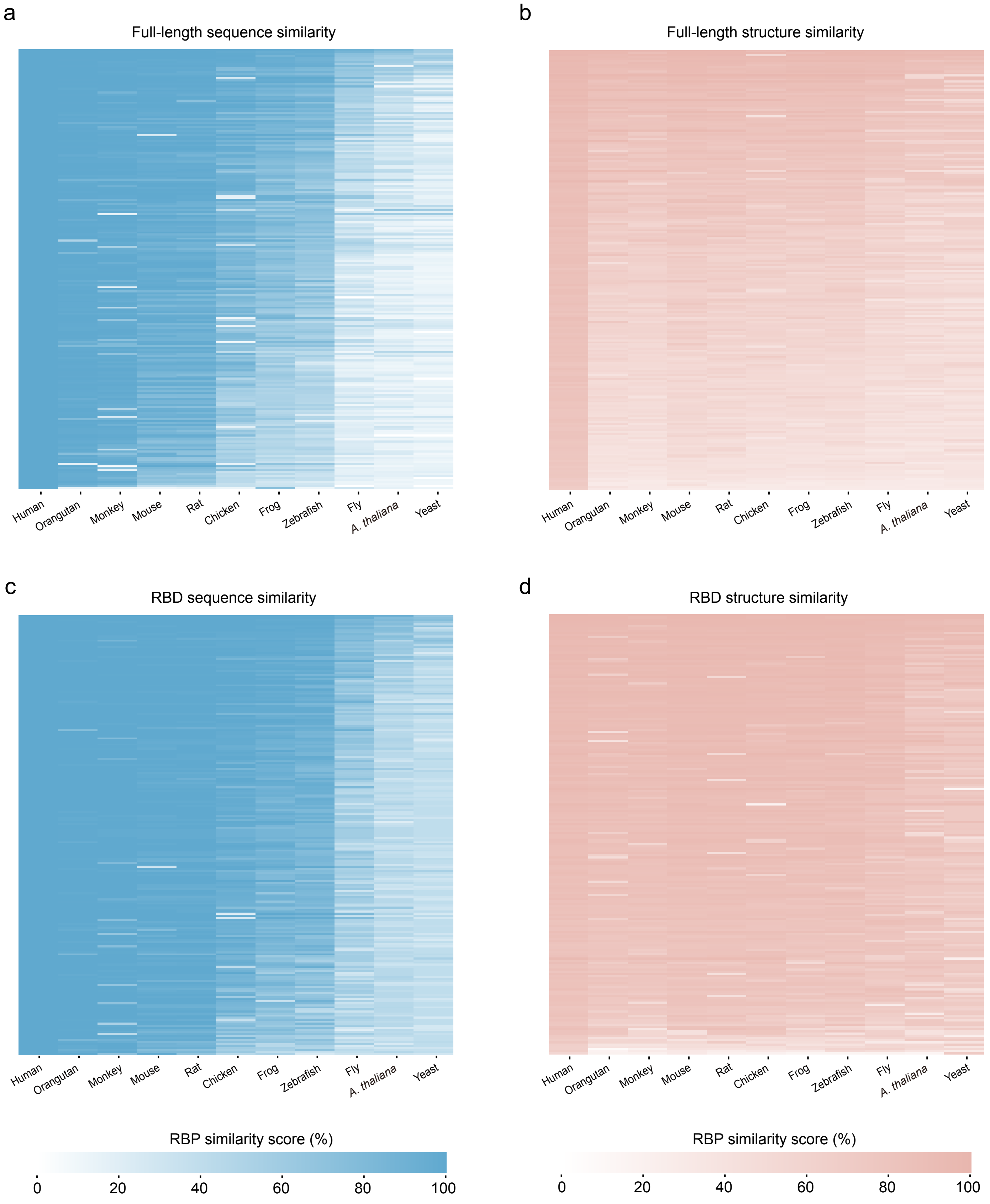
a
Full-length sequence similarity
b
Full-length structure similarity
c
RBD sequence similarity
d
RBD structure similarity
Human
Orangutan
Monkey
Mouse
Rat
Chicken
Frog
Zebrafish
Fly
A. thaliana
Yeast
RBP similarity score (%)
0
20
40
60
80
100
RBP similarity score (%)
0
20
40
60
80
100

Figure S2

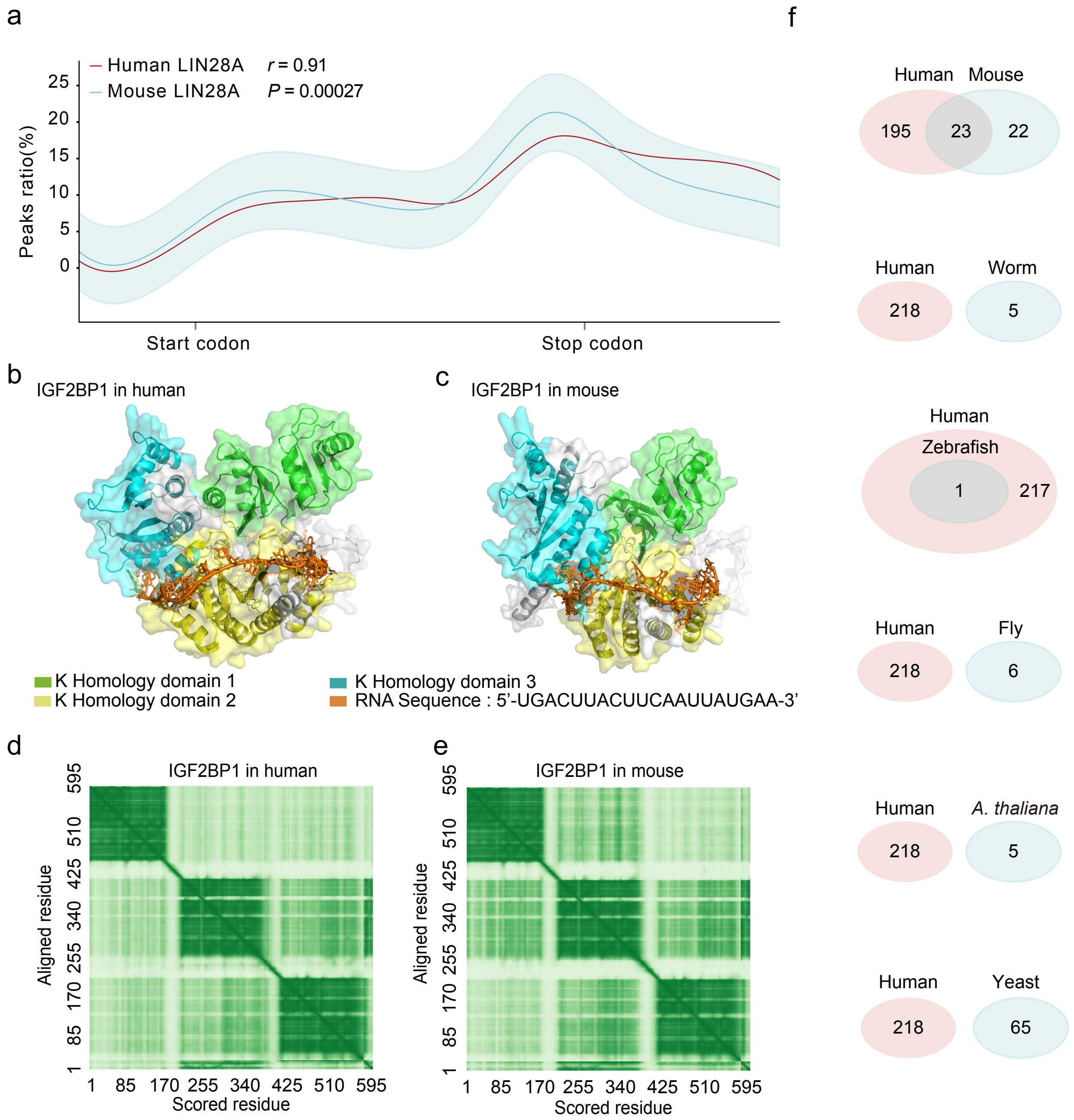
a
Human LIN28A
Mouse LIN28A
r = 0.91
P = 0.00027
Peaks ratio(%)
25
20
15
10
5
0
Start codon
Stop codon
b
IGF2BP1 in human
c
IGF2BP1 in mouse
🟩 K Homology domain 1
🟨 K Homology domain 2
🟦 K Homology domain 3
🟧 RNA Sequence : 5'-UGACUUACUUCAAUUAUGAA-3'
d
IGF2BP1 in human
Aligned residue
595
510
425
340
255
170
85
1
1 85 170 255 340 425 510 595
Scored residue
e
IGF2BP1 in mouse
Aligned residue
595
510
425
340
255
170
85
1
1 85 170 255 340 425 510 595
Scored residue
f
Human
Mouse
195
23
22
Human
Worm
218
5
Human
Zebrafish
1
217
Human
Fly
218
6
Human
A. thaliana
218
5
Human
Yeast
218
65

Figure S3

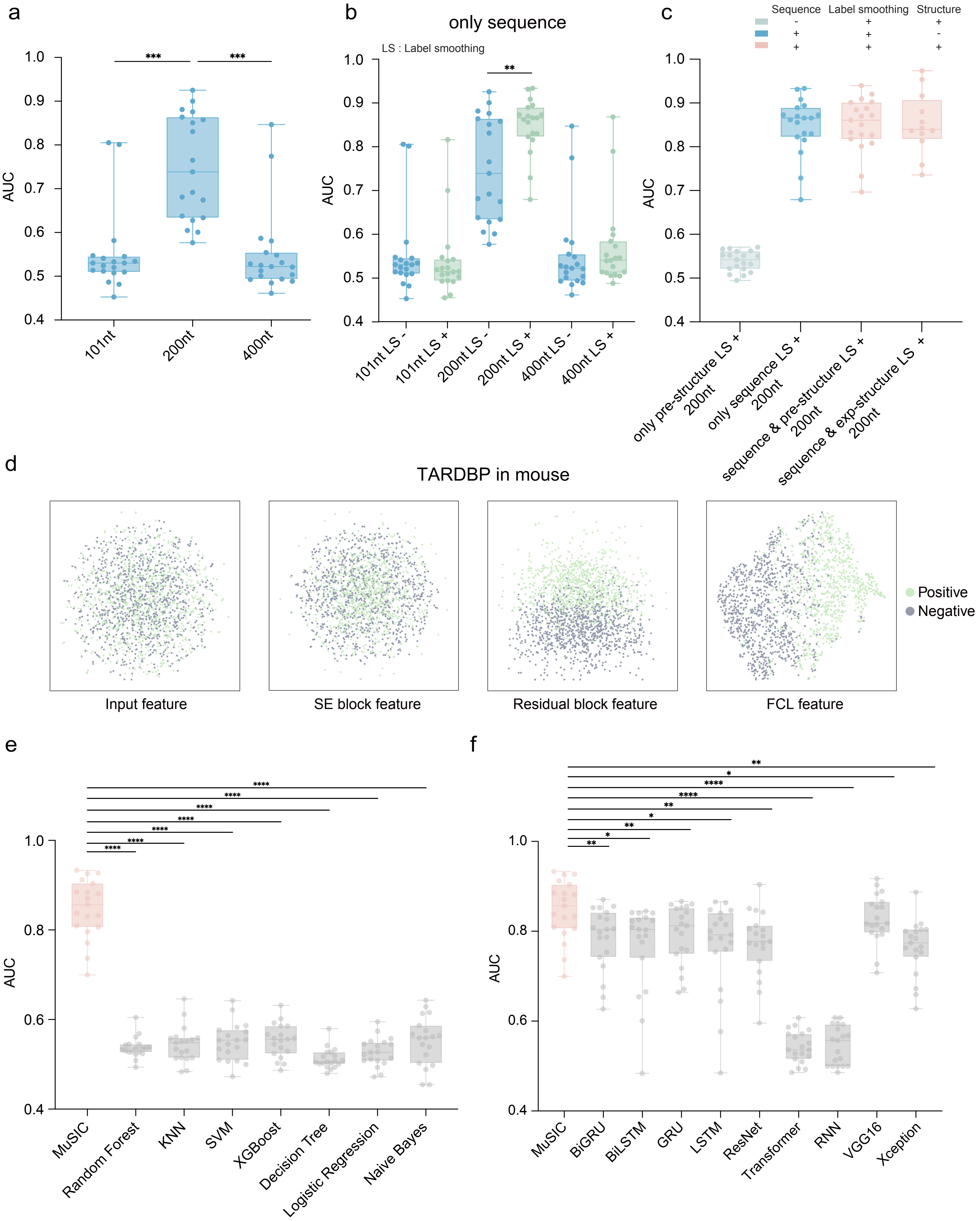
a
AUC
1.0
0.9
0.8
0.7
0.6
0.5
0.4
***
***
101nt
200nt
400nt
b
only sequence
LS : Label smoothing
**
101nt LS -
101nt LS +
200nt LS -
200nt LS +
400nt LS -
400nt LS +
c
Sequence
Label smoothing
Structure
- + +
+ + -
+ + +
only pre-structure LS + 200nt
only sequence LS + 200nt
sequence & pre-structure LS + 200nt
sequence & exp-structure LS + 200nt
d
TARDBP in mouse
Input feature
SE block feature
Residual block feature
FCL feature
Positive
Negative
e
****
MuSIC
Random Forest
KNN
SVM
XGBoost
Decision Tree
Logistic Regression
Naive Bayes
f
**
*
****
MuSIC
BiGRU
BiLSTM
GRU
LSTM
ResNet
Transformer
RNN
VGG16
Xception

Figure S4

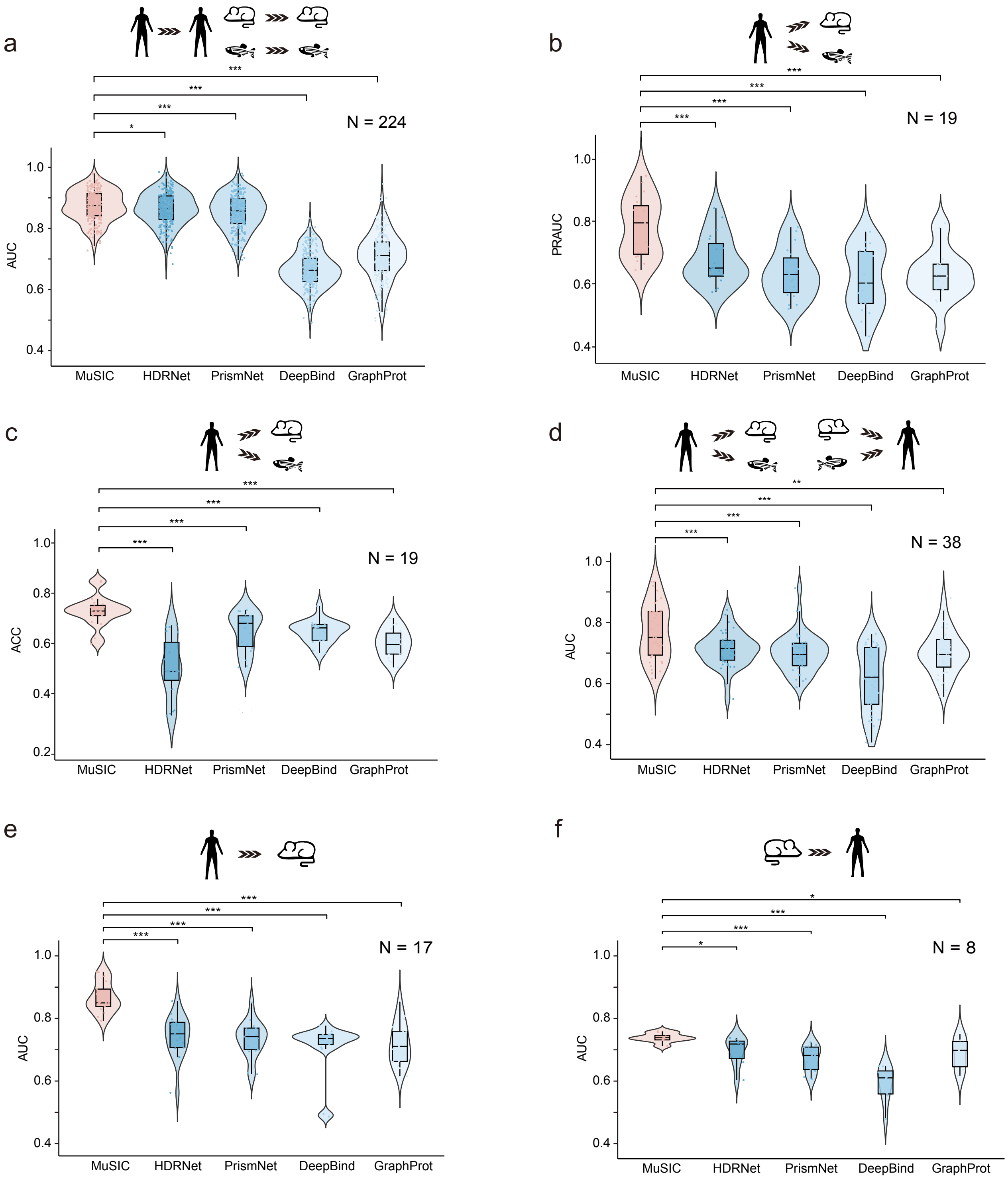
a
***
***
***
*
N = 224
AUC
1.0
0.8
0.6
0.4
MuSIC
HDRNet
PrismNet
DeepBind
GraphProt
b
***
***
***
***
N = 19
PRAUC
1.0
0.8
0.6
0.4
MuSIC
HDRNet
PrismNet
DeepBind
GraphProt
c
***
***
***
***
N = 19
ACC
1.0
0.8
0.6
0.4
0.2
MuSIC
HDRNet
PrismNet
DeepBind
GraphProt
d
**
***
***
***
N = 38
AUC
1.0
0.8
0.6
0.4
MuSIC
HDRNet
PrismNet
DeepBind
GraphProt
e
***
***
***
***
N = 17
AUC
1.0
0.8
0.6
0.4
MuSIC
HDRNet
PrismNet
DeepBind
GraphProt
f
*
***
***
*
N = 8
AUC
1.0
0.8
0.6
0.4
MuSIC
HDRNet
PrismNet
DeepBind
GraphProt

Figure S5

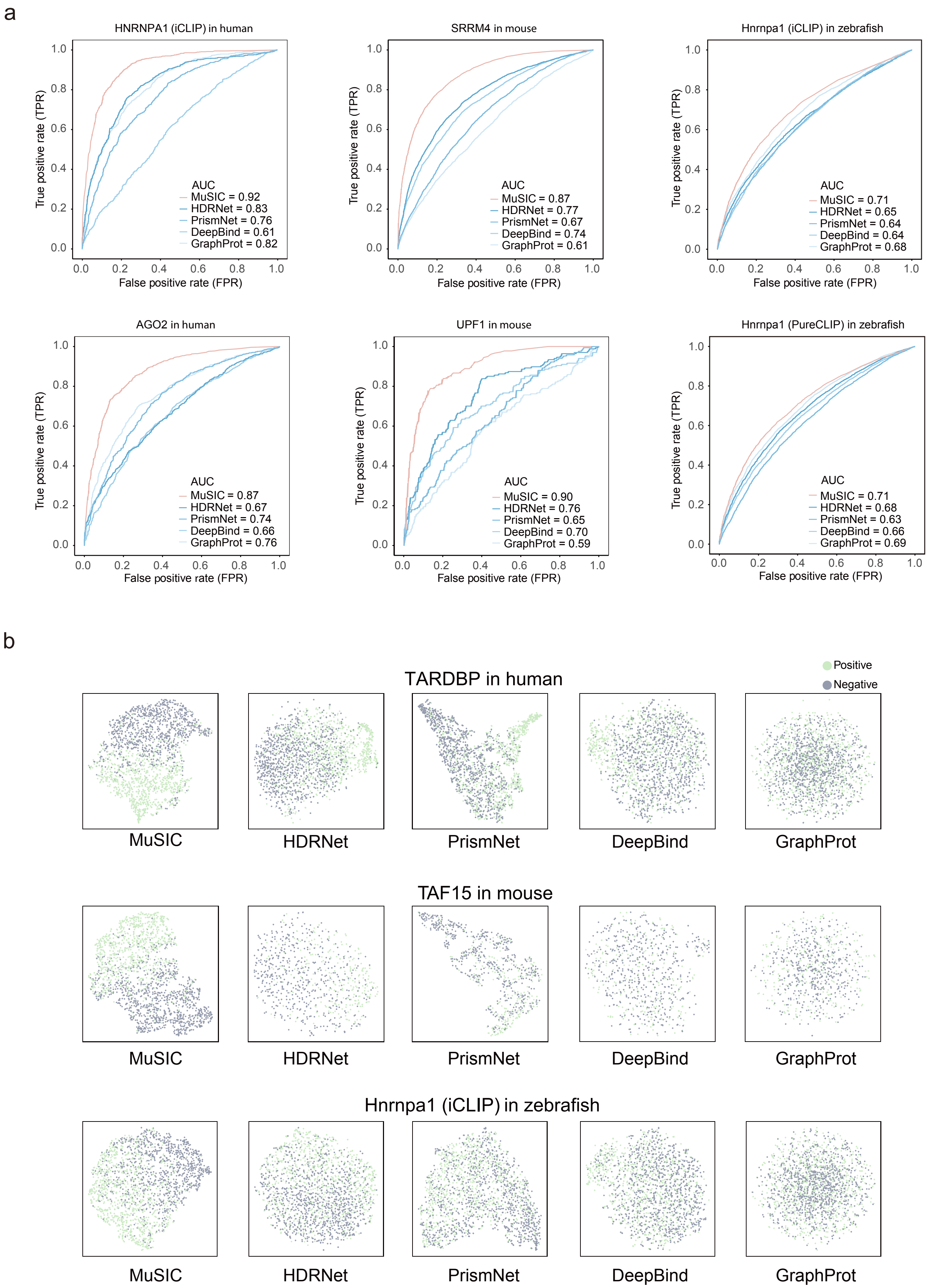
a
HNRNPA1 (iCLIP) in human
True positive rate (TPR)
False positive rate (FPR)
AUC
MuSIC = 0.92
HDRNet = 0.83
PrismNet = 0.76
DeepBind = 0.61
GraphProt = 0.82
SRRM4 in mouse
AUC
MuSIC = 0.87
HDRNet = 0.77
PrismNet = 0.67
DeepBind = 0.74
GraphProt = 0.61
Hnrnpa1 (iCLIP) in zebrafish
AUC
MuSIC = 0.71
HDRNet = 0.65
PrismNet = 0.64
DeepBind = 0.64
GraphProt = 0.68
AGO2 in human
AUC
MuSIC = 0.87
HDRNet = 0.67
PrismNet = 0.74
DeepBind = 0.66
GraphProt = 0.76
UPF1 in mouse
AUC
MuSIC = 0.90
HDRNet = 0.76
PrismNet = 0.65
DeepBind = 0.70
GraphProt = 0.59
Hnrnpa1 (PureCLIP) in zebrafish
AUC
MuSIC = 0.71
HDRNet = 0.68
PrismNet = 0.63
DeepBind = 0.66
GraphProt = 0.69
0.0
0.2
0.4
0.6
0.8
1.0
b
Positive
Negative
TARDBP in human
MuSIC
HDRNet
PrismNet
DeepBind
GraphProt
TAF15 in mouse
MuSIC
HDRNet
PrismNet
DeepBind
GraphProt
Hnrnpa1 (iCLIP) in zebrafish
MuSIC
HDRNet
PrismNet
DeepBind
GraphProt

Figure S6

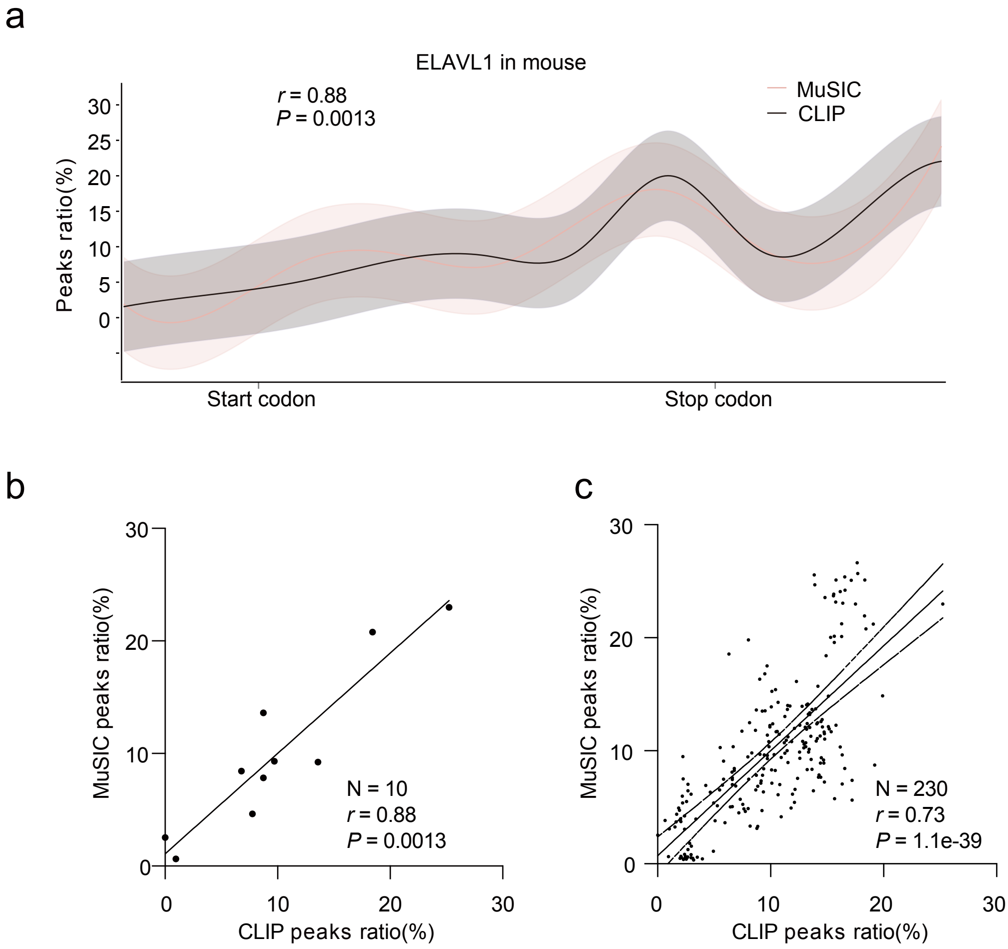
a
ELAVL1 in mouse
r = 0.88
P = 0.0013
MuSIC
CLIP
Peaks ratio(%)
30
25
20
15
10
5
0
Start codon
Stop codon
b
MuSIC peaks ratio(%)
CLIP peaks ratio(%)
N = 10
r = 0.88
P = 0.0013
0
10
20
30
c
MuSIC peaks ratio(%)
CLIP peaks ratio(%)
N = 230
r = 0.73
P = 1.1e-39
0
10
20
30

Figure S7

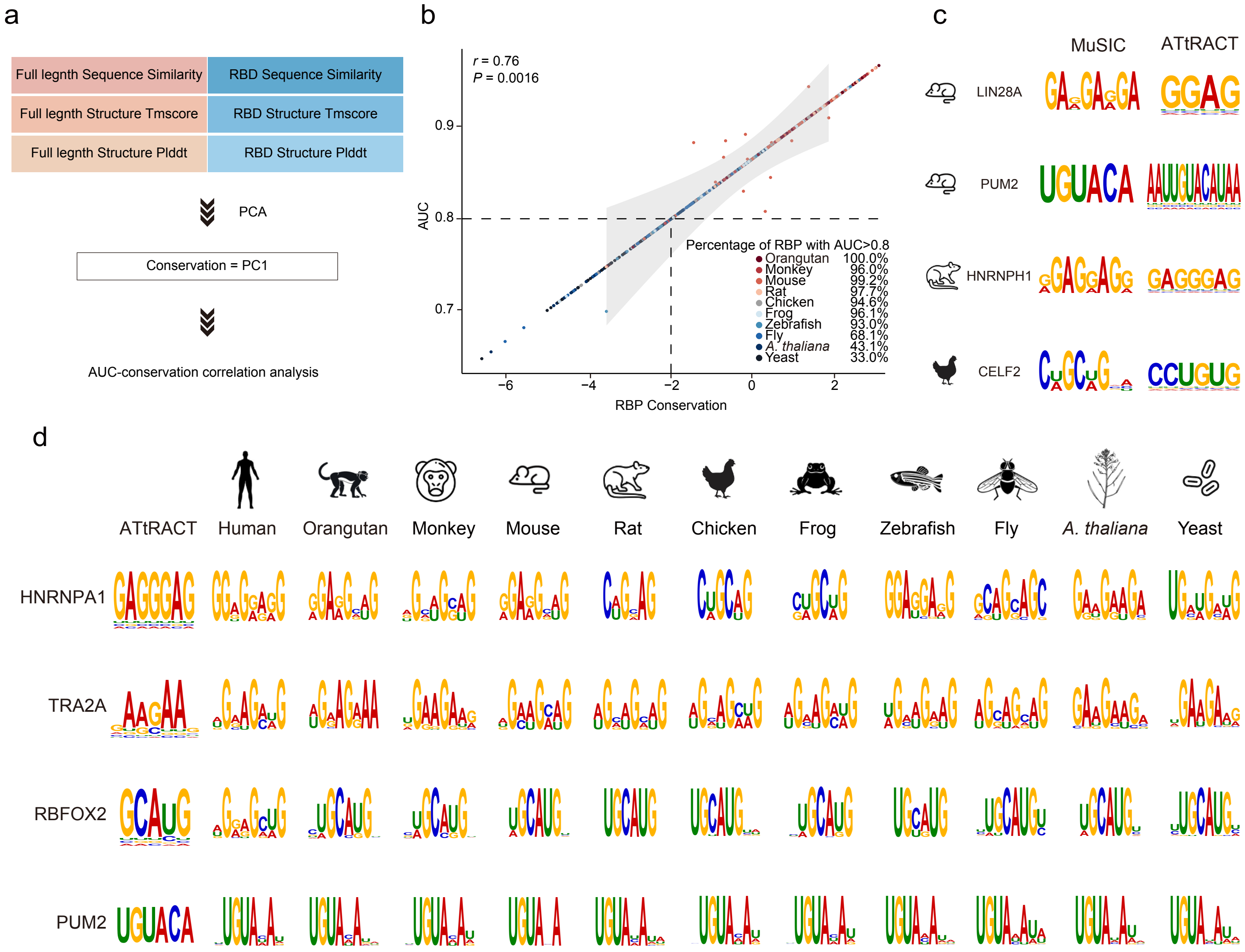
a
Full legnth Sequence Similarity
RBD Sequence Similarity
Full legnth Structure Tmscore
RBD Structure Tmscore
Full legnth Structure Plddt
RBD Structure Plddt
PCA
Conservation = PC1
AUC-conservation correlation analysis
b
r = 0.76
P = 0.0016
AUC
0.9
0.8
0.7
RBP Conservation
−6
−4
−2
0
2
Percentage of RBP with AUC>0.8
Orangutan 100.0%
Monkey 96.0%
Mouse 99.2%
Rat 97.7%
Chicken 94.6%
Frog 96.1%
Zebrafish 93.0%
Fly 68.1%
A. thaliana 43.1%
Yeast 33.0%
c
MuSIC
ATtRACT
LIN28A
PUM2
HNRNPH1
CELF2
d
ATtRACT
Human
Orangutan
Monkey
Mouse
Rat
Chicken
Frog
Zebrafish
Fly
A. thaliana
Yeast
HNRNPA1
TRA2A
RBFOX2
PUM2

Figure S8

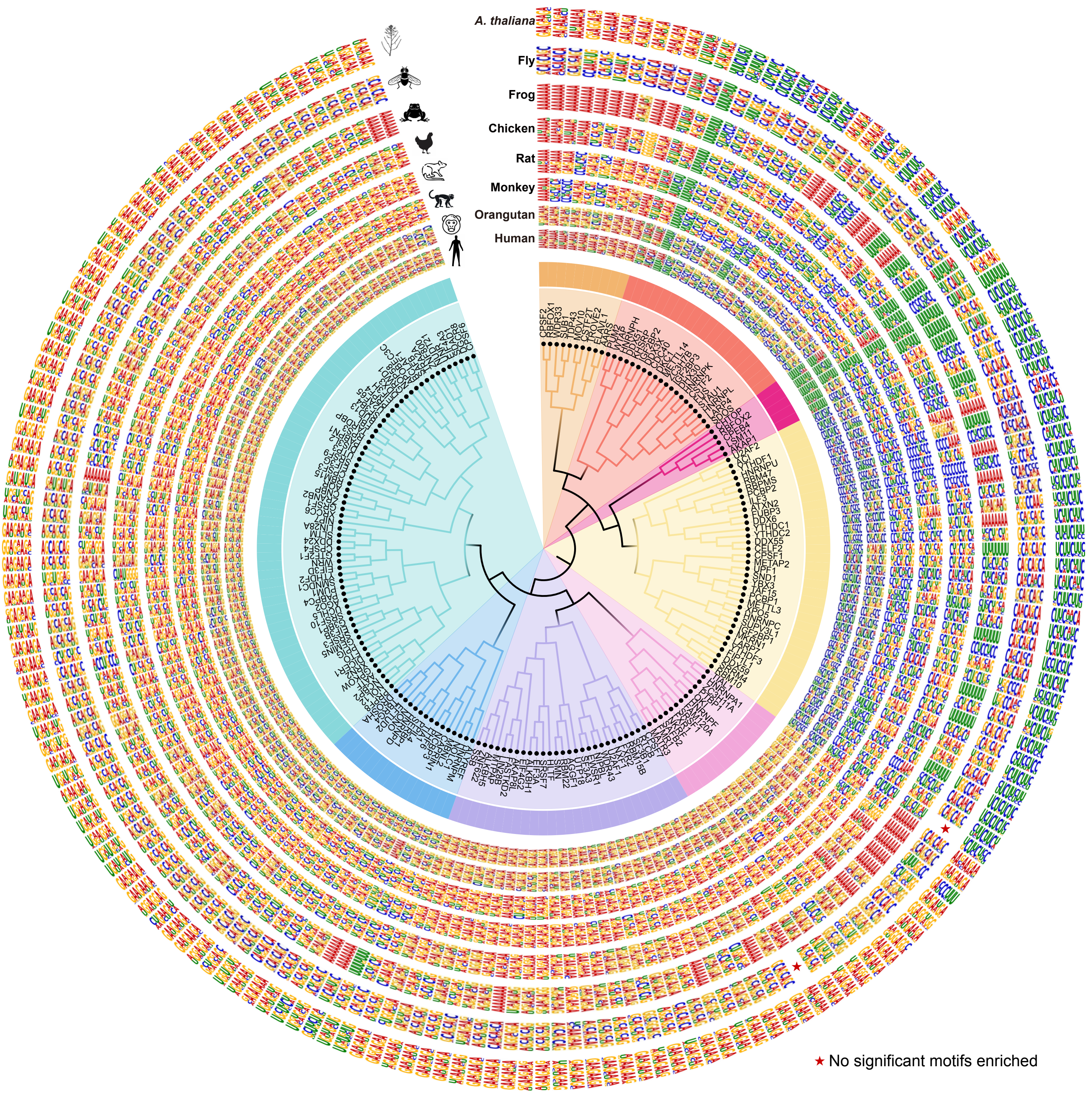

★ No significant motifs enriched

Figure S9

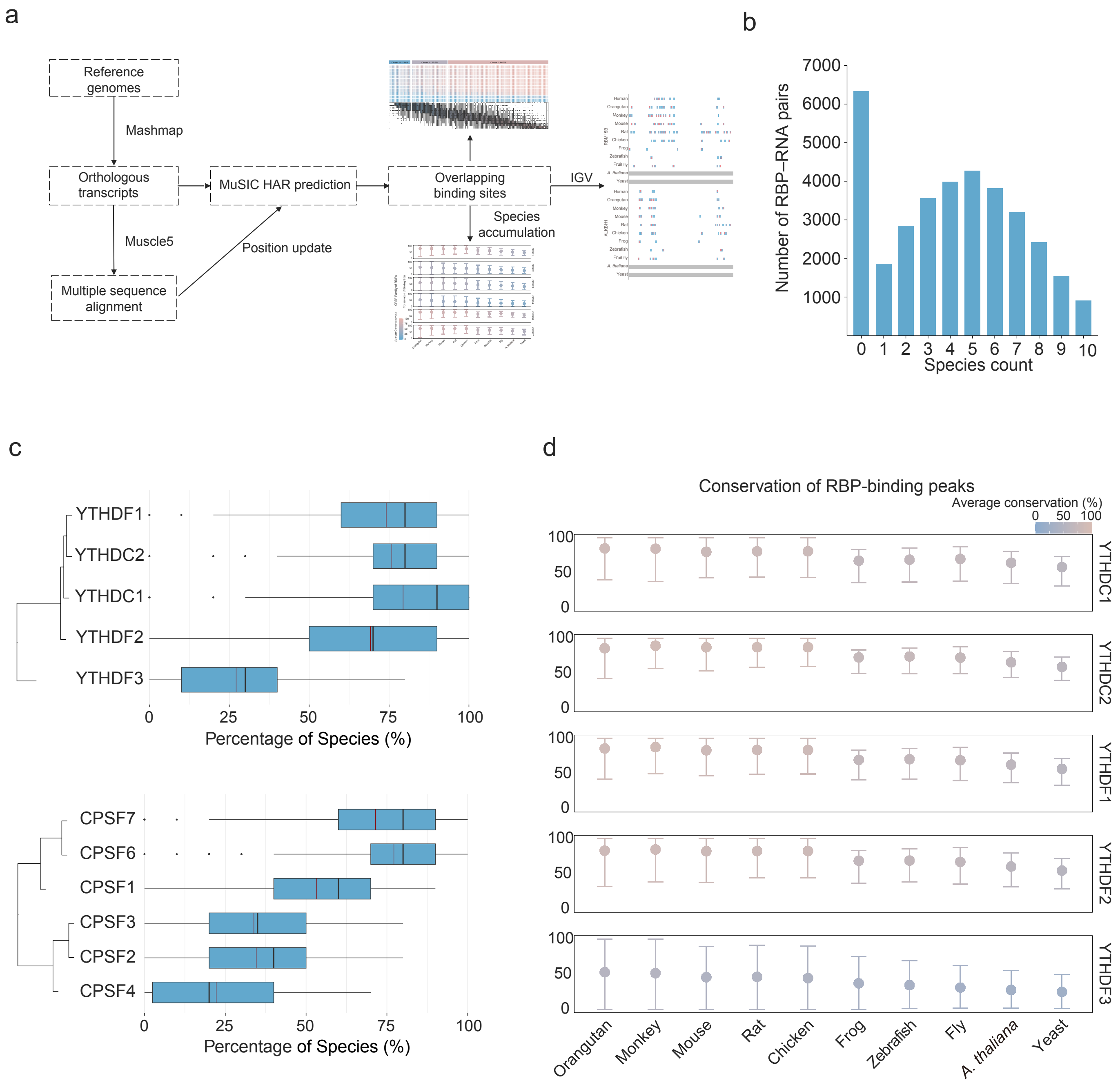
a
Reference genomes
Mashmap
Orthologous transcripts
Muscle5
Multiple sequence alignment
MuSIC HAR prediction
Position update
Overlapping binding sites
Species accumulation
IGV
b
7000
6000
5000
4000
3000
2000
1000
Number of RBP–RNA pairs
0 1 2 3 4 5 6 7 8 9 10
Species count
c
YTHDF1
YTHDC2
YTHDC1
YTHDF2
YTHDF3
0 25 50 75 100
Percentage of Species (%)
CPSF7
CPSF6
CPSF1
CPSF3
CPSF2
CPSF4
0 25 50 75 100
Percentage of Species (%)
d
Conservation of RBP-binding peaks
Average conservation (%)
0 50 100
100
50
0
YTHDC1
YTHDC2
YTHDF1
YTHDF2
YTHDF3
Orangutan
Monkey
Mouse
Rat
Chicken
Frog
Zebrafish
Fly
A. thaliana
Yeast

Figure S10

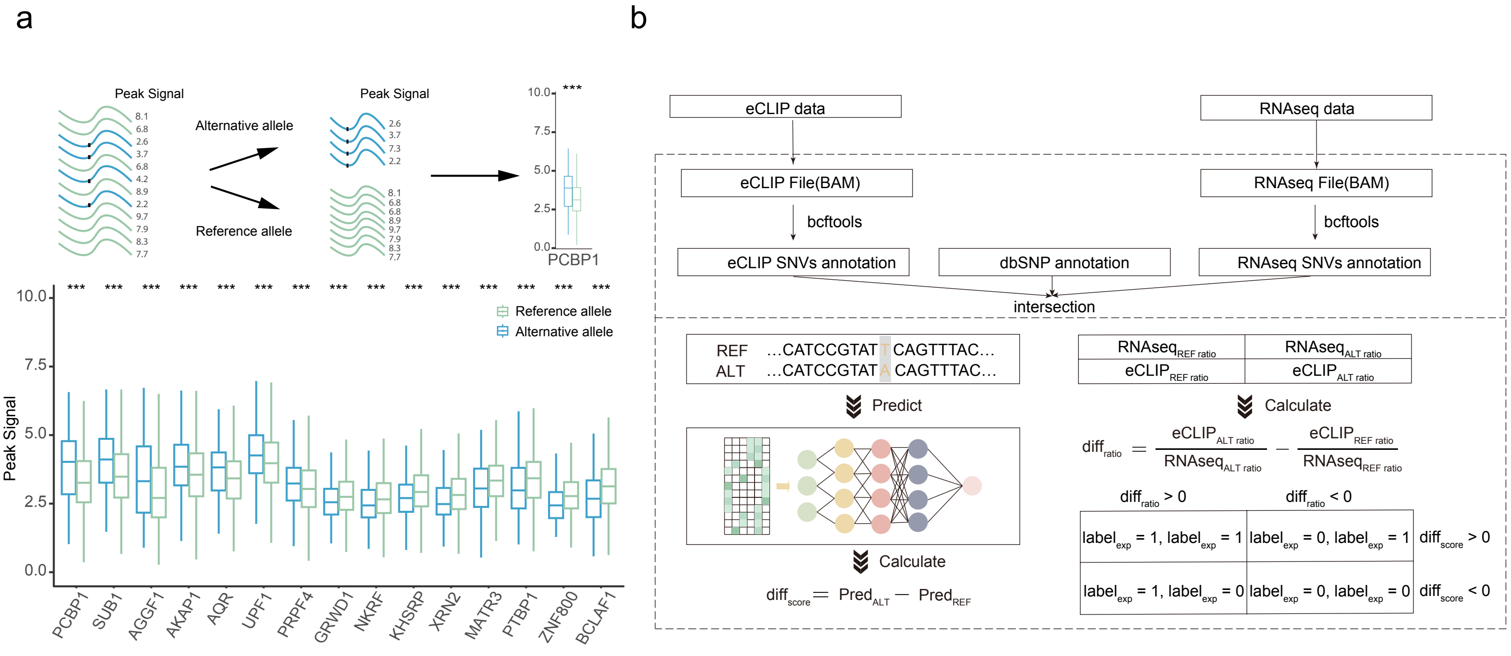
a
Peak Signal
8.1
6.8
2.6
3.7
6.8
4.2
8.9
2.2
9.7
7.9
8.3
7.7
Alternative allele
Reference allele
Peak Signal
2.6
3.7
7.3
2.2
8.1
6.8
6.8
8.9
9.7
7.9
8.3
7.7
10.0
7.5
5.0
2.5
0.0
***
PCBP1
10.0
7.5
5.0
2.5
0.0
Peak Signal
Reference allele
Alternative allele
PCBP1
SUB1
AGGF1
AKAP1
AQR
UPF1
PRPF4
GRWD1
NKRF
KHSRP
XRN2
MATR3
PTBP1
ZNF800
BCLAF1
b
eCLIP data
RNAseq data
eCLIP File(BAM)
RNAseq File(BAM)
bcftools
bcftools
eCLIP SNVs annotation
dbSNP annotation
RNAseq SNVs annotation
intersection
REF ...CATCCGTAT T CAGTTTAC...
ALT ...CATCCGTAT A CAGTTTAC...
Predict
Calculate
$diff_{score} = Pred_{ALT} - Pred_{REF}$
$RNAseq_{REF\ ratio}$
$RNAseq_{ALT\ ratio}$
$eCLIP_{REF\ ratio}$
$eCLIP_{ALT\ ratio}$
Calculate
$diff_{ratio} = \frac{eCLIP_{ALT\ ratio}}{RNAseq_{ALT\ ratio}} - \frac{eCLIP_{REF\ ratio}}{RNAseq_{REF\ ratio}}$
$diff_{ratio} > 0$
$diff_{ratio} < 0$
$label_{exp} = 1, label_{exp} = 1$
$label_{exp} = 0, label_{exp} = 1$
$diff_{score} > 0$
$label_{exp} = 1, label_{exp} = 0$
$label_{exp} = 0, label_{exp} = 0$
$diff_{score} < 0$

Figure S11

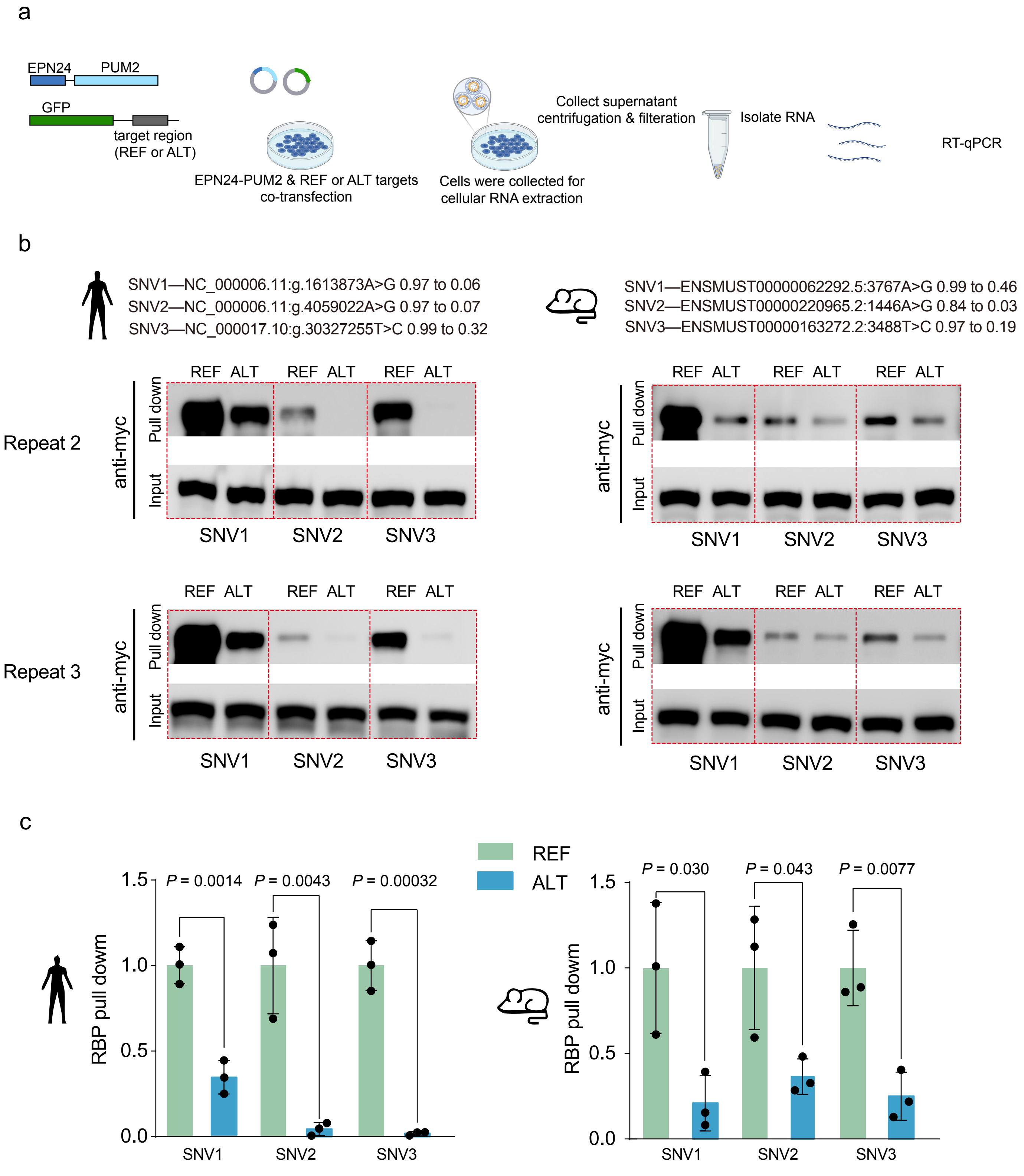
a
EPN24
PUM2
GFP
target region
(REF or ALT)
EPN24-PUM2 & REF or ALT targets
co-transfection
Cells were collected for
cellular RNA extraction
Collect supernatant
centrifugation & filteration
Isolate RNA
RT-qPCR
b
SNV1—NC_000006.11:g.1613873A>G 0.97 to 0.06
SNV2—NC_000006.11:g.4059022A>G 0.97 to 0.07
SNV3—NC_000017.10:g.30327255T>C 0.99 to 0.32
SNV1—ENSMUST00000062292.5:3767A>G 0.99 to 0.46
SNV2—ENSMUST00000220965.2:1446A>G 0.84 to 0.03
SNV3—ENSMUST00000163272.2:3488T>C 0.97 to 0.19
Repeat 2
Repeat 3
anti-myc
Pull down
Input
REF ALT REF ALT REF ALT
SNV1 SNV2 SNV3
c
REF
ALT
RBP pull dowm
1.5
1.0
0.5
0.0
P = 0.0014
P = 0.0043
P = 0.00032
P = 0.030
P = 0.043
P = 0.0077
SNV1
SNV2
SNV3

Figure S12

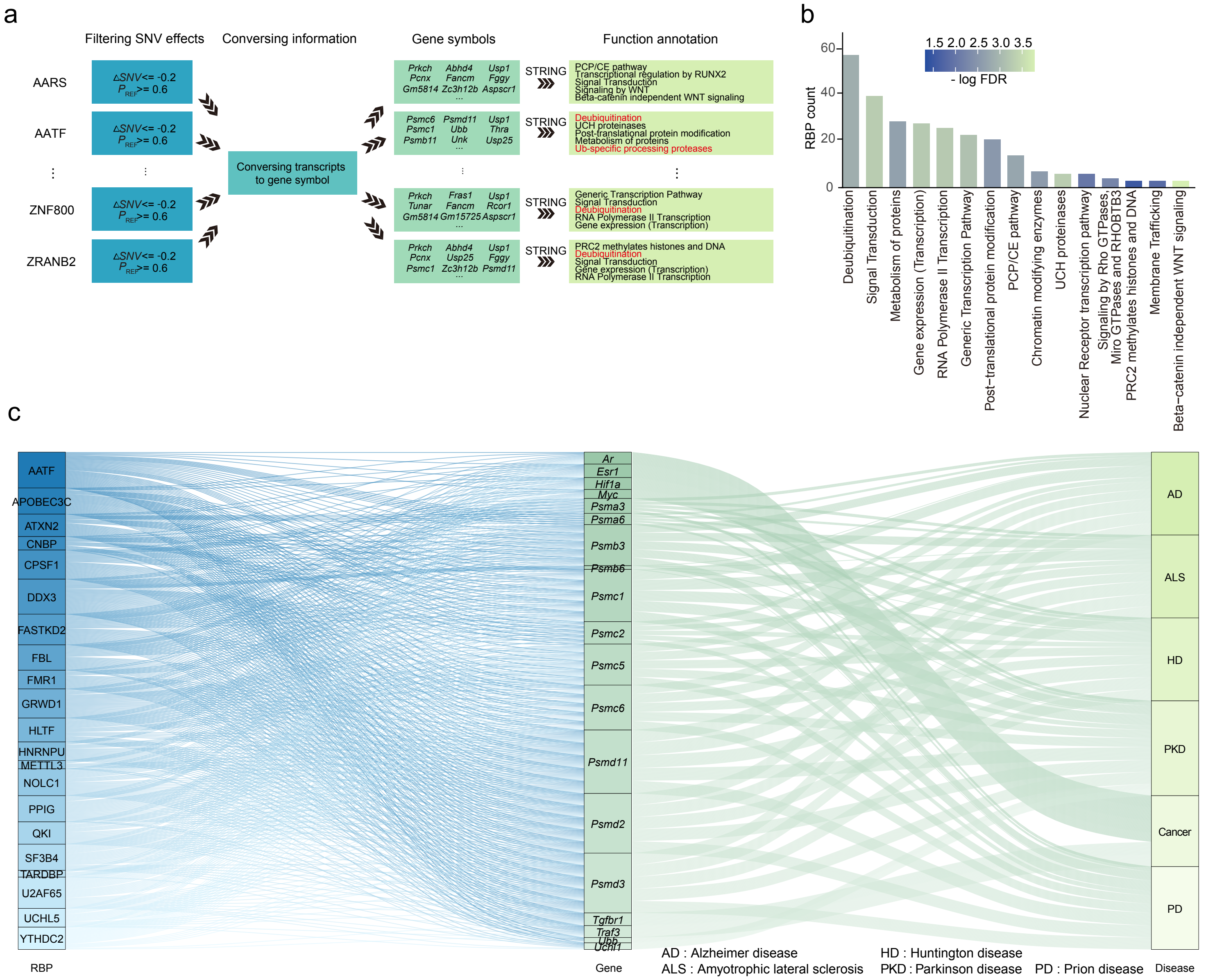
a
Filtering SNV effects
Conversing information
Gene symbols
Function annotation
AARS
AATF
⋮
ZNF800
ZRANB2
ΔSNV<= -0.2
P_REF>= 0.6
Conversing transcripts to gene symbol
Prkch Abhd4 Usp1 Pcnx Fancm Fggy Gm5814 Zc3h12b Aspscr1 …
Psmc6 Psmd11 Usp1 Psmc1 Ubb Thra Psmb11 Unk Usp25 …
Prkch Fras1 Usp1 Tunar Fancm Rcor1 Gm5814 Gm15725 Aspscr1 …
Prkch Abhd4 Usp1 Pcnx Usp25 Fggy Psmc1 Zc3h12b Psmd11 …
STRING
PCP/CE pathway
Transcriptional regulation by RUNX2
Signal Transduction
Signaling by WNT
Beta-catenin independent WNT signaling
Deubiquitination
UCH proteinases
Post-translational protein modification
Metabolism of proteins
Ub-specific processing proteases
Generic Transcription Pathway
Signal Transduction
Deubiquitination
RNA Polymerase II Transcription
Gene expression (Transcription)
PRC2 methylates histones and DNA
Deubiquitination
Signal Transduction
Gene expression (Transcription)
RNA Polymerase II Transcription
b
RBP count
0
20
40
60
1.5 2.0 2.5 3.0 3.5
- log FDR
Deubiquitination
Signal Transduction
Metabolism of proteins
Gene expression (Transcription)
RNA Polymerase II Transcription
Generic Transcription Pathway
Post-translational protein modification
PCP/CE pathway
Chromatin modifying enzymes
UCH proteinases
Nuclear Receptor transcription pathway
Signaling by Rho GTPases, Miro GTPases and RHOBTB3
PRC2 methylates histones and DNA
Membrane Trafficking
Beta-catenin independent WNT signaling
c
AATF
APOBEC3C
ATXN2
CNBP
CPSF1
DDX3
FASTKD2
FBL
FMR1
GRWD1
HLTF
HNRNPU
METTL3
NOLC1
PPIG
QKI
SF3B4
TARDBP
U2AF65
UCHL5
YTHDC2
RBP
Ar
Esr1
Hif1a
Myc
Psma3
Psma6
Psmb3
Psmb6
Psmc1
Psmc2
Psmc5
Psmc6
Psmd11
Psmd2
Psmd3
Tgfbr1
Traf3
Ubb
Uchl1
Gene
AD
ALS
HD
PKD
Cancer
PD
Disease
AD : Alzheimer disease
ALS : Amyotrophic lateral sclerosis
HD : Huntington disease
PKD : Parkinson disease
PD : Prion disease

Figure S13

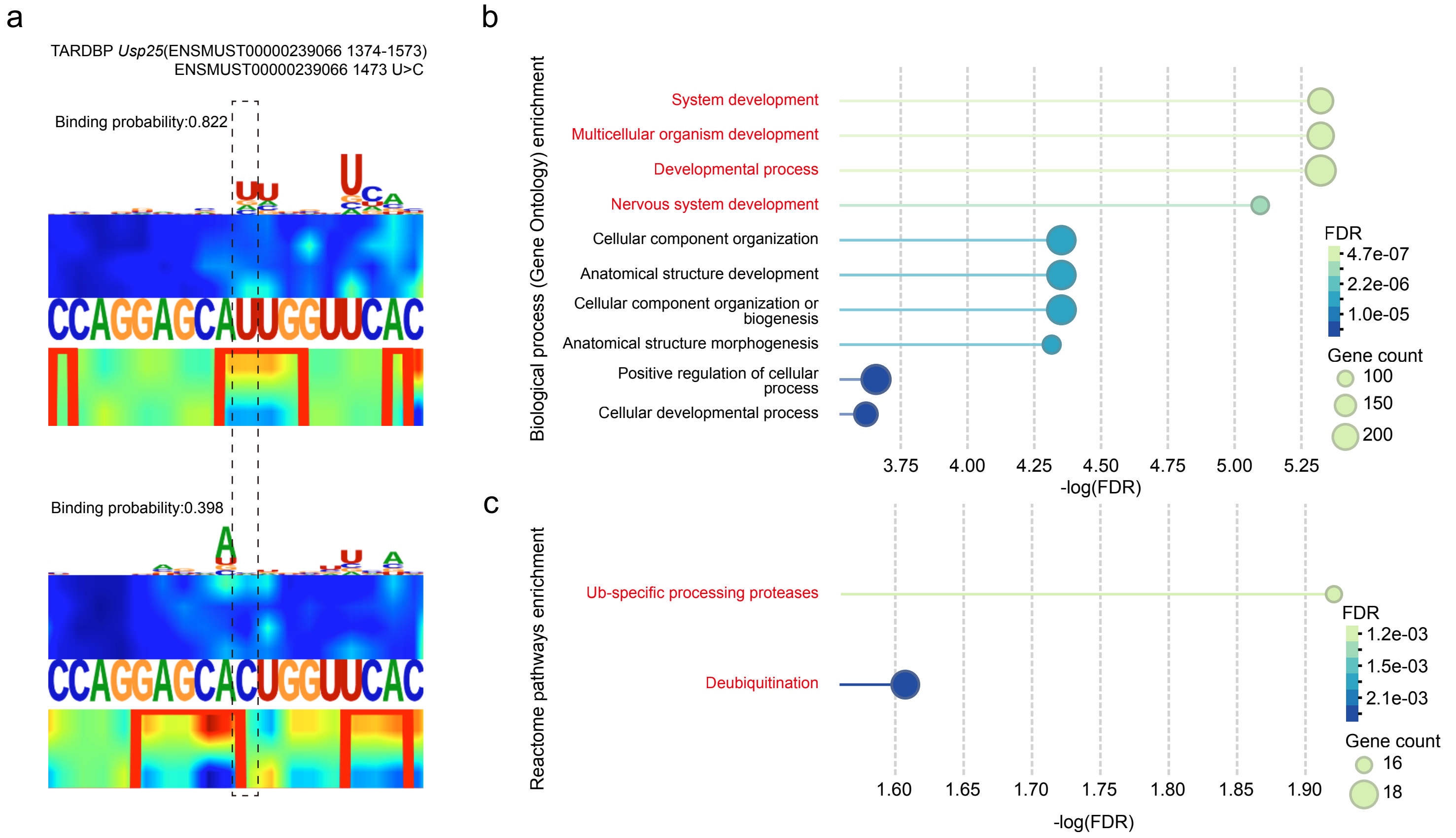
a
TARDBP Usp25(ENSMUST00000239066 1374-1573)
ENSMUST00000239066 1473 U>C
Binding probability:0.822
CCAGGAGCAUUGGUUCAC
Binding probability:0.398
CCAGGAGCACUGGUUCAC
b
Biological process (Gene Ontology) enrichment
System development
Multicellular organism development
Developmental process
Nervous system development
Cellular component organization
Anatomical structure development
Cellular component organization or biogenesis
Anatomical structure morphogenesis
Positive regulation of cellular process
Cellular developmental process
3.75
4.00
4.25
4.50
4.75
5.00
5.25
-log(FDR)
FDR
4.7e-07
2.2e-06
1.0e-05
Gene count
100
150
200
c
Reactome pathways enrichment
Ub-specific processing proteases
Deubiquitination
1.60
1.65
1.70
1.75
1.80
1.85
1.90
-log(FDR)
FDR
1.2e-03
1.5e-03
2.1e-03
Gene count
16
18